UNIVERSITÀ DEGLI STUDI DI PADOVA

Dipartimento di Fisica e Astronomia "Galileo Galilei"

Master Degree in Physics

Final Dissertation

Multinucleon transfer reactions in the ^{206}Pb + ^{118}Sn system studied with the PRISMA spectrometer

Thesis supervisor

Dr. Lorenzo Corradi

Thesis co-supervisor

Prof. Giovanna Montagnoli

Dr. Tea Mijatović

Candidate

Ablaihan Utepov

Academic Year 2018/2019

Abstract

Multinucleon transfer reactions were measured in the ^{206}Pb + ^{118}Sn system to study nucleon-nucleon correlation properties, whose information will be extracted via the transfer probabilities for one and two neutron transfers in an energy range from above to well below the Coulomb barrier. The aim of this thesis was to identify the nuclear charges of the Sn-like transfer products by analyzing the data at the highest measured bombarding energy (E_{lab}=1200).

The measurement of the transfer products was carried out with the large acceptance PRISMA spectrometer at θ_{lab}=25° and 35°. After a sophisticated analysis procedure, the mass-integrated proton channels ranging from (-7p) to (+6p) and from (-8p) to (+5p) for the measurements at θ_{lab}=25° and 35°, respectively, were identified.

The extracted yields were compared with the semi-classical model GRAZING whose prediction that the proton stripping path is more favoured than the pick-up one was confirmed by the measurements at both angles. In the comparison with the previously studied ^{197}Au+^{130}Te [1] heavy system, our data were much more underestimated giving us insight into the dominance of the deep-inelastic components as a result of the used higher bombarding energy. In this way, it is expected that at the lower energies the deep-inelastic components will be strongly reduced and the quasi-elastic components will be much more dominant providing the best condition for the nucleon-nucleon correlation studies.

The data at lower bombarding energies, where it will be especially important to distinguish pure proton and pure neutron transfer channels, will be the subject of future studies. In this context, the present thesis serves also as a solid basis for such a challenging job.

Acknowledgements

I would like to thank all of those who have supported me for the past two years of my graduate studies.

My master thesis supervisor, Dr. Lorenzo Corradi, internship supervisor, Dr. Dieter Ackermann, and my tutor during the first year of master, Dr. Jose Antonio Lay, for guidance, for support and for a great contribution to my theoretical and practical knowledge.

The NucPhys coordinators, Prof. Giovanna Montagnoli, Dr. Alberto Stefanini, Prof. Francesca Gulminelli and Prof. Jose Arias, for academic support and for opportunities provided this master program.

My sincere thanks to the collaborators from the Ruđer Bošcović Institute, Prof. Suzana Szilner, Dr. Tea Mijatović, Dr. Lovro Palaversa and Dr. Petra Čolović, for their warm hospitality during my stay in Zagreb.

I would like to express my deepest appreciation to Dr. Alain Goasduff, Dr. Franco Galtarossa and Dr. Marc-Olivier Frégeau for an assistance in data analysis.

Special thanks to Christa Buoso for precious guidance and support.

On a more personal note, I would like to thank my friends and my family for encouragement and supporting my efforts throughout these years.

Contents

List of Figures

9

List of Tables

12

Chapter 1

Introduction

One of the main goals of nuclear physics is to understand the structure of nuclei and their properties. Nuclear reaction studies aim to reach this goal through different reaction mechanisms. In particular, heavy-ion collisions performed at energies around the Coulomb barrier open many possible applications of transfer reactions like, for example, defining the properties of nucleon-nucleon correlations.

Two-nucleon transfer reactions induced by the pairing interaction are a unique tool to investigate the nucleon-nucleon correlations in nuclei. Several experiments performed in the past were explained mainly via the extraction of enhancement coefficients providing a direct information of the correlation of the populated states [20]. Unfortunately, the experimental evidence was marred by the fact that the most of the existing studies involved inclusive cross sections at energies higher than the Coulomb barrier and at angles forward of the grazing [21], where the interplay between nuclear attraction and Coulomb repulsion complicates the reaction mechanism.

With the recent construction of the new generation large solid angle spectrometers, one can gain more than one order of magnitude in overall efficiency compared to the conventional devices preserving good ion identification also using bombarding energies below the Coulomb barrier, where interacting nuclei are at very large distances and the influence of the nuclear attraction can be easily accounted for [7]. This is one of the reasons which led to the renewal of the interest in transfer reactions which could be used in the study of nuclear structure and the nuclear reaction dynamics.

The use of transfer reactions with light ions provided evidence on the construction of shell model and on the study of the properties of nucleon-nucleon correlation in the nuclear medium. In very recent years, considerable progress has been made

in the exploiting of multinucleon transfer reactions with heavy ions at the energies around the Coulomb barrier which gave opportunity to study the relative role of single-particle and pair-transfer modes [10].

The possibility of probing pair correlations in heavy-ion collisions has been an open questions for many years. In more recent years the use of the large acceptance magnetic spectrometer PRISMA in combination with the inverse kinematics condition allowed to extract the quantitative information on the nucleon-nucleon correlation by employing the experimental spectroscopic factors and the correct nuclear structure information. For the first time in a heavy-ion collision, the one neutron and the two neutron transfer reactions were described, without introducing any enhancement factor for two neutron transfer, in the ^{116}Sn + ^{60}Ni system by including all the necessary information on the entrance and on the exit channel in the reaction mechanism. In this system the ground to ground state Q-values for one-neutron and two-neutron transfers were very close to optimum ($Q_{opt} \sim 0$) which made the reaction feasible to study. The data were represented by the transfer probability (P_{tr}), defined as ratio of the neutron transfer cross section to the corresponding Rutherford cross section. The employed theoretical microscopic calculation very well reproduced the experimental data, in particular the transfer probabilities for the one and two neutron channels showed good agreement in absolute value and slope [7].

In the collision amongst very heavy ions, the influence of nucleon-nucleon correlations in the evolution of the reaction is not well known and it could be modified significantly due to the population of highly excited final states and angular momentum in the presence of high Coulomb field. It would be interesting to investigate the behavior of the transfer probabilities for one-neutron and two-neutron transfers, the break of pairing interaction and the Q-value dependence of the transfer cross sections. For a proper comparison with already studied systems, the ^{206}Pb + ^{118}Sn system is an excellent candidate having a semi-magic combination, with closed proton shells and open neutron shells, with the ground to ground state Q-values for neutron transfers close to optimum. In addition, this system meets the requirement to be detected with high enough resolution in A, Z and Q-value [9].

Within this context, an experiment of multinucleon transfer reaction of ^{206}Pb + ^{118}Sn system at three different energies around the Coulomb barrier, namely at E_{lab}=1200, 1090 and 1035 MeV in inverse kinematics, was performed. The reaction products were measured with the PRISMA spectrometer at two different angles, namely at θ_{lab}=25° and 35°, covering a wide range of the distance of closest approach

corresponding to the various transfer probabilities for both neutron and proton stripping and pick-up channels.

As a first step in this very complex analysis it is essential to focus on the bombarding energy above the Coulomb barrier since at this energy one can have the highest kinetic energies of the outgoing ions and the highest cross section of the transfer products, in particular for the proton transfer channels, with the best Z resolution in the IC. The thesis is therefore aimed at the identification of the nuclear charge Z of the Sn-like reaction products of the measurement at the highest energies at both angles. The extracted yields of mass-integrated proton transfer channels will be compared with theoretical calculation based on the GRAZING model which predicts for this system the population of multinucleon transfer channels in both proton pick-up and stripping directions.

The performed procedure of data analysis for this thesis, which includes the calibration of the PRISMA detectors, can be used as a solid basis for future work incorporating the full reconstruction of atomic mass, nuclear charge and Q-value of the reaction products.

Chapter 2

Generals on transfer reactions with heavy ions

In this Chapter, heavy-ion collisions at energies close to the Coulomb barrier will be discussed, particularly focusing on multinucleon transfer reactions (MNT). Then the results of the recently performed experiments on the MNT reactions will be presented. Later, few theoretical concepts used to describe the transfer processes will be outlined.

2.1   Heavy-ion reactions near the Coulomb barrier

Nuclear reactions are an extremely complicated many-body quantum mechanical processes which depend on the structure of the involved nuclei and on the reaction mechanism. The variety of processes involved in the collision can be classified according to the timescales, impact parameters, involved masses, transferred angular momenta and kinetic energies. A simplified sketch of the various reaction mechanisms induced in heavy-ion collisions at the energies around the Coulomb barrier is shown in Figure 2.1. Increasing the impact parameter the interaction of heavy-ions evolves from fusion reactions, through deep inelastic processes, to quasi-elastic reactions. The elastic scattering dominates for distant collision where nuclei feel only Coulomb force.

Although the number of processes involved in heavy-ion reactions is large, some concepts such as the major role played by the Coulomb force are common to all of them.

Some of the basic features of heavy-ion reactions can be understood in terms of an interaction potential U(r) between the centers of mass of the two colliding nuclei
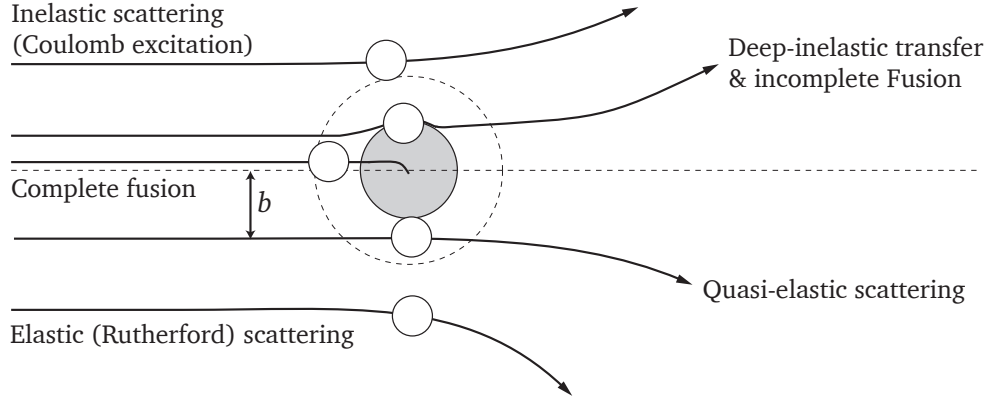
Figure 2.1: Classification of the reaction mechanisms between heavy ions as a function of the impact parameter [2].

A and B consisting of a Coulomb repulsion $U_C(r)$, a short-range nuclear attraction $U_n(r)$ and a centrifugal potential $U_l(r)$. The Coulomb potential $U_C(r)$ by using two point charges Z_A and Z_B is expressed as

$$U_C(r) = \frac{Z_A Z_B e^2}{r} \tag{2.1}$$

The nuclear interaction $U_n(r)$ is often represented by a Woods-Saxon potential with depth U_0, the inverse diffuseness $1/a$ and the nuclear radii $R_i = (1.20 A_i^{1/3} - 0.08)$ fm:

$$U_n(r) = -\frac{U_0}{1 + \exp[(r - R_A - R_B)/a]} \tag{2.2}$$

The centrifugal potential $U_l(r)$ with the angular momentum l, the reduced Planck constant $\hbar = 6.582 \times 10^{-16}$ eVs and the reduced mass $\mu = (A_A \cdot A_B)/(A_A + A_B)$ is written as

$$U_l(r) = \frac{l(l+1)\hbar^2}{2\mu r^2} \tag{2.3}$$

In this way, the basic form of the effective radial potential U(r) can be defined as

$$U(r) = U_C(r) + U_n(r) + U_l(r)$$

$$= \frac{Z_A Z_B e^2}{r} + \frac{U_0}{1 + \exp[(r - R_A - R_B)/a]} + \frac{l(l+1)\hbar^2}{2\mu r^2}$$

(2.4)

In head-on collisions (l=0), when the two nuclei are not too heavy ($A_A \cdot A_B < 23400$), this potential shows a maximum, called Coulomb barrier, at a relative distance r_B determined by:

$$\left(\frac{\partial U(r)}{\partial r}\right)_{r=r_B} = 0$$

where r_B can be calculated from the masses A_A and A_B of the nuclei [3]. For trajectories with non-zero impact parameters b≠0 the corresponding angular momenta are defined as $L_b = b\sqrt{2\mu_{AB}E_{cm}}$. Increasing the impact parameter b leads to increasing the angular momentum L_b, given that the bombarding energy E_{cm} is fixed. For high values of L_b the centrifugal potential becomes so steep that the maximum nuclear attraction is not able to produce a barrier like, for example, the case of ^{40}Ca+^{40}Ca shown in Figure 2.2.
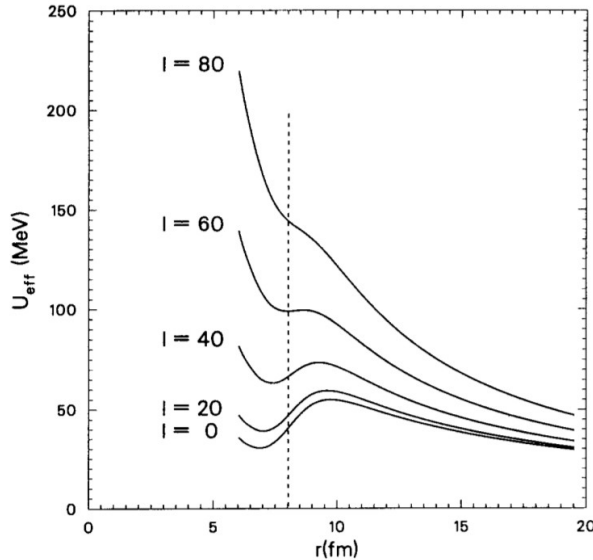
Figure 2.2: Effective radial potential for ^{40}Ca+^{40}Ca for different angular momenta l. The sum of the nuclear radii indicated by a dashed line. One can note that for high l-values the barrier essentially vanishes [3].

For heavier systems, like for the ^{208}Pb+^{118}Sn reaction studied in this thesis with $A_{\text{Pb}} \cdot A_{\text{Sn}} \sim 24000$, the Coulomb barrier vanishes already for low values of L$_b$ since the maximum attractive force is not sufficiently strong to compensate for the Coulomb repulsion. In a macroscopic picture, this implies that the system cannot form a compound nucleus even for impact parameters close to 0 [3]. Nevertheless, the interacting nuclei can come into close contact for a short period of time during which a transfer of many nucleons and a loss of the kinetic energy can take place.

2.1.1 Multinucleon transfer reactions

In this kind of processes, the projectile and target exchange one or more nucleons, and both pick-up and stripping reactions may occur. The degrees of freedom associated to the exchanging nucleons are very important in understanding the evolution from the quasi-elastic to the more complex deep-inelastic regime in the heavy-ion reactions close to Coulomb barrier.

In the quasi-elastic reactions, a change between initial and final mass partitions of the system is very little. The interaction time is very short (10^{-23}-10^{-22} s) during which the projectile losses only moderate amount of kinetic energy and exchanges only few nucleons with the target. It is assumed that the incident particle interacts at the surface of the target keeping their identity. This allows the extraction of the spectroscopic factors and provides information on correlations [22].

The deep-inelastic reactions are characterized by a massive transfer of nucleons and a very large dissipation of incident kinetic energy. This energy is mainly converted into intrinsic excitation of the reaction fragments. In these reactions, the primary products have a binary character as a result of the longer interaction time than that of quasi-elastic reactions. But the reaction time is not long enough to fuse into compound nucleus. The exiting fragments exhibit (broader) bell shaped angular distributions with a peak close to the grazing angle. This means that the process is very fast while the large energy losses indicate that there are large deformations of the two ions. Taking into account these two, short collision time and large energy losses, it is suggested that in the evolution of the reaction the excitation of surface modes plays an important role being the low-lying modes the main source for the formation of the large deformations [10].

In the multinucleon transfer reactions (MNT), the amount of dissipated kinetic energy can be understood qualitatively in a very simple way. Let us imagine a system for which N independent single-particle transitions can occur all with the same

probability p. Then the probability, in such a system, to have the transfer of n particles is simply given by the binomial distribution:

$$P_n = \binom{N}{n} p^n (1-p)^{N-n} \qquad (2.5)$$

For the above distribution the average number of transferred particles is $\langle n \rangle = pN$ so that the corresponding average energy loss is $\langle E_{loss} \rangle = \langle n \rangle Q$.

In heavy-ion collisions, an average number of transferred nucleons of the order of 10 and around 5 MeV average energy loss for each transition result in the energy loss for the transfer process of the order of 50 MeV. This example shows the importance of the dissipation of energy due to the transfer of many nucleons.

The grazing angle mentioned above is defined as scattering angle when the distance of closest approach between two nuclei is very close to the sum of their radii [23]. The yield of the MNT reactions reach the maximum at this angle, usually having bell shaped angular distributions. However, one should keep in mind that the shape can change depending on the bombarding energy. For example, at deep subbarrier energies the bell shape can vanish, being the maximum of the distribution at $\theta_{cm}=180°$.

2.1.2 Recent experimental results on multi-nucleon transfer reactions

In the last decade, the renewed interest in transfer reactions has been mainly due to the realization that MNT reactions could be used to populate nuclei moderately rich in neutrons [24, 25]. This renewed interest benefited from the construction of the new generation large solid angle spectrometers based on trajectory reconstruction, providing at the same time large overall efficiency and good identification of reaction products.

MNT reactions are a very powerful tool for the population of neutron rich nuclei moderately far from stability. As an example, Figure 2.3 demonstrates the mass and charge distribution of Ca-like transfer products in the ^{40}Ca+^{208}Pb reaction at E_{lab}=235 MeV at the grazing angle [4]. The most intense band corresponds to the beam-like fragments with Z=20 and A=40. One can notice that the transfer products with approximately 6 neutron pick-up and 6 proton stripping were observed at this bombarding energy. They are shown with the two dashed lines corresponding to pure neutron pick-up and pure proton stripping channels, while the full line

represents the charge equilibrium, namely the location of the N/Z ratio of the compound nucleus. One observes that the final nuclei are on the left side of this line favouring only the proton stripping and the neutron pick-up processes. These is the indication of the dominance of a direct mechanism in the population of different fragments.
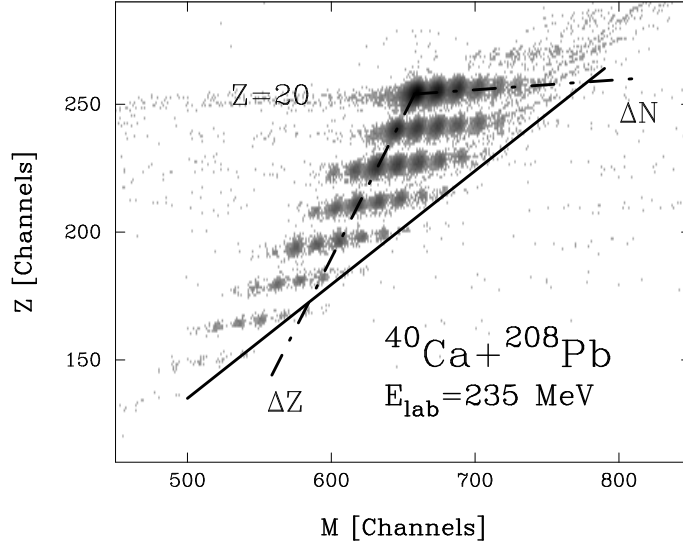
Figure 2.3: Left: Mass-charge distribution of Ca-like transfer products in the ^{40}Ca+^{208}Pb reaction at E_{lab}=235 MeV. The dash-dotted lines correspond to the pure proton stripping (ΔZ) and to the pure neutron pick-up (ΔN) channels. [4].

From the reaction mechanism point of view, MNT reactions can be useful to describe the evolution of the heavy-ion reaction from the quasi-elastic to the more complicated deep inelastic regimes. Figure 2.4 shows the experimental angular distributions, integrated over the full TKEL, for the indicated transfer channels in the reaction ^{40}Ar+^{208}Pb at E_{lab}= 6.41 MeV/A (see Section 2.2.3) [5]. The evolution of the reaction dynamics, moving from forward to backward angles, starts with an increase of the transfer cross section due to the progressive overlap of the interacting nuclei and then the cross section decreases because of the absorption effects as a result of opening of various competing channels. The angular distributions for one and two nucleon transfers have a bell shape centered at the grazing angle (θ_{gr}=54°) and depend weakly on the isotope as it is expected in the quasi-elastic regime. One can see that the distributions broaden and increase at forward angles when the transfer of more nucleons take place, especially for the proton pick-up channels. This is the clear indication of the contribution from the deep-inelastic regime.
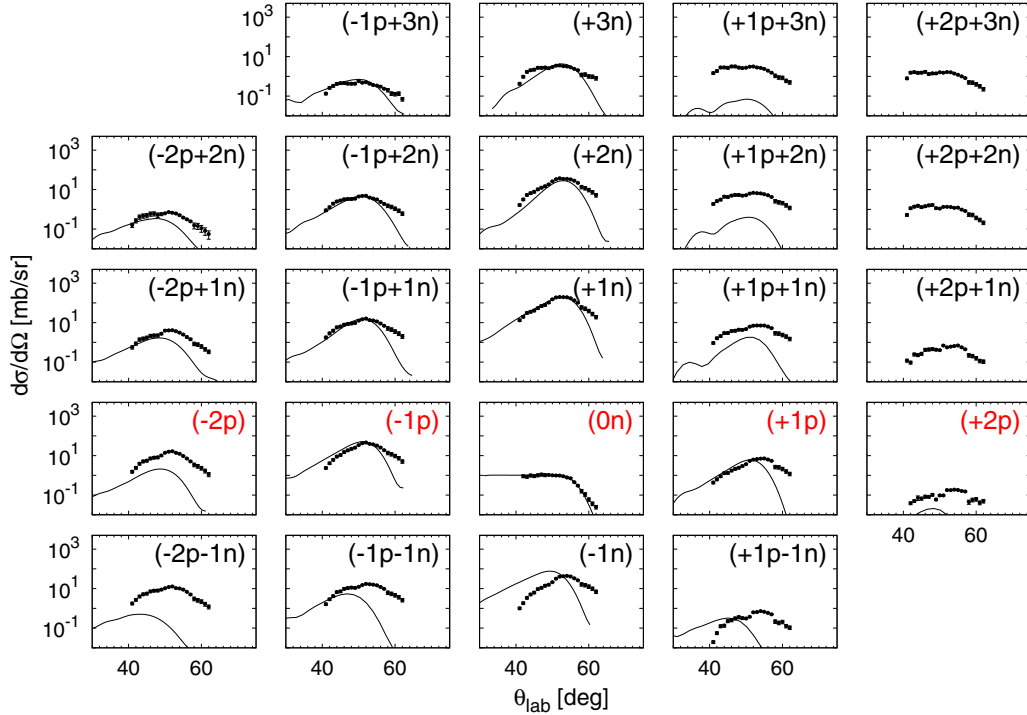
Figure 2.4: Experimental (points) and GRAZING calculated (curves) Q-value integrated angular distributions for the indicated transfer channels in the reaction ^{40}Ar+^{208}Pb at E_{lab}= 6.41 MeV/A. The (0n) channel corresponds to the elastic (+inelastic) channel, plotted as a ratio to the Rutherford cross section [5].

Transfer reactions play an essential role in the study of the structure of nuclei. With light-ion reactions, they gave considerable inputs to the construction of shell model and to establish the properties of nucleon-nucleon correlations. How pair correlations can be probed in heavy ion collisions, is still an open question. Several experiments have been performed in the recent years aiming at the probing the ability of two nucleons in heavy ion transfer reactions to form pairs of zero angular momentum. Figure 2.5 shows the experimental transfer probabilities P_{tr} as a function of distance of closest approach D for one and two neutron transfer channels in MNT reactions ^{96}Zr+^{40}Ca (left) and ^{60}Ni+^{116}Sn (middle) at near barrier energies performed in inverse kinematics (measured by PRISMA) [6, 7]. The transfer probabilities P_{tr} are extracted from the experimental cross sections by the following formula

$$P_{tr} = \frac{d\sigma_{tr}}{d\sigma_{Ruth}} \tag{2.6}$$
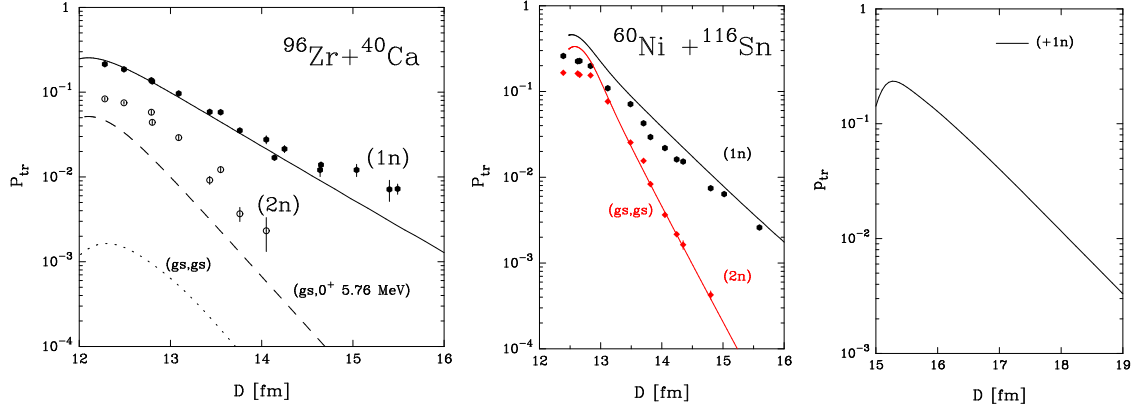
Figure 2.5: Left: Experimental (points) and microscopically calculated (lines) transfer probabilities as a function of the distance of closest approach D for one and two neutron transfer channels in the ^{96}Zr+^{40}Ca (left) system. The full line represents the inclusive probability for one neutron transfer, the dotted line is the ground-ground state transition for the two-neutron transfer and the dash line is the transition to the first 0^+ excited state at 5.76 MeV in ^{42}Ca [6]. Middle: Experimental (points) and microscopically calculated (lines) transfer probabilities for the one and two-neutron pick-up channels in the ^{60}Ni+^{116}Sn reaction [7]. Right: Calculated transfer probabilities for one neutron transfer channel in the ^{206}Pb+^{118}Sn reaction of the present thesis [8, 9]

and plotted as a function of the distance of closest approach D for a Coulomb trajectory

$$D = \frac{Z_a\ Z_A\ e^2}{2E_{cm}} \left(1 + \frac{1}{\sin(\theta_{cm}/2)}\right) \tag{2.7}$$

In the ^{96}Zr+^{40}Ca system, experimental transfer probabilities P_{tr} for the ground to ground state transitions deviate by $\sim$2 orders of magnitude from data. By incorporating high energy 0^+ states one reduces the deviation from data to a factor $\sim$3. Residual deviation is probably caused by states with large angular momentum populated in the reaction so that more complicated two-particle correlations have to be taken into account.

In the ^{60}Ni+^{116}Sn system, the experimental transfer probabilities P_{tr} are well reproduced, for the first time with heavy ion reactions, in absolute values and in slope

by microscopic calculations which incorporate nucleon-nucleon pairing correlations.

Being the subject of this thesis Figure 2.5 (right) shows the calculated transfer probabilities for one neutron transfer channel in the ^{206}Pb+^{118}Sn reaction. Extracting the experimental transfer probabilities P_{tr} for this reaction would shed light to the effect of nucleon-nucleon correlations in the evolution of the reaction in the presence of high Coulomb fields and would check the ability of the calculations to reproduce data.

2.2 Theoretical approach to transfer reactions

Several theoretical studies have been performed in order to understand the reaction dynamics of the transfer processes induced by heavy-ions at the energies near the Coulomb barrier. Among these are the perturbation theory, the quantal coupled-channel and the semi-classical approaches. Using the first one can describe one-nucleon transfer in first order approximation and two-nucleon transfer in second order approximation [21]. The last two will be briefly described, focusing in particular on the semi-classical model GRAZING, in this section. It will also present the dependence of the cross sections on the Q-value mentioned in the previous chapter.

2.2.1 The quantal coupled-channel approach

The quantal coupled-channels approach is at the base for any description of direct reaction processes [10]. In this approach the various reaction channels such as inelastic, transfer etc. are treated as not independent of each other. So in order to obtain information on a particular channel one has to consider the contribution of the other channels. The relative importance of the different channels is represented by a *form factor* which is the matrix elements between initial and final states of the reaction process. These matrix elements can be obtained by solving the time-dependent Schrödinger equation

$$i\hbar\frac{\partial}{\partial t}\Psi(t) = H\Psi(t) \tag{2.8}$$

The total wavefunction $|\Psi\rangle$ of the system is expanded in terms of exit channel wavefunctions $|\psi_\beta\rangle = |\psi_b\psi_B\rangle$ and is expressed as

$$\Psi(t) = \sum_{\beta} c_{\beta}(t) \, \psi_{\beta}(t) \, e^{-iE_{\beta}t/\hbar} \tag{2.9}$$

where the time-dependent coefficient $c_{\beta}(t)$ defines the amplitude to be in channel β.

The Hamiltonian is given as

$$H = H_b + H_B + T_{bB} + V_{bB}$$

where the single Hamiltonians H_b and H_B stand for the intrinsic states of the two ions, the kinetic term $T_{bB} = -\hbar^2 \nabla_{bB}^2/2m_{bB}$ accounts for the relative motion, and the effective interaction V_{bB} refers to the coupling interaction between the colliding nuclei.

Inserting Equation 2.9 in Equation 2.8, one finally obtains the following system of coupled equations:

$$i\hbar\dot{c}_{\beta}(t) = \sum_{\gamma} \langle \omega_{\beta}| \, V_{\gamma} - U_{\gamma} \, |\psi_{\gamma}\rangle \, e^{i(E_{\beta}-E_{\gamma})t/\hbar} \, c_{\gamma}(t) \tag{2.10}$$

where the vectors $|\omega_{\xi}\rangle$ constitute a dual base introduced to overcome the problem of the non-orthogonality of the vectors $|\psi_{\gamma}\rangle$. Formally:

$$\omega_{\xi} = \sum_{\gamma} g_{\xi\gamma}^{-1} \, \psi_{\gamma} \, ,$$

where g^{-1} is reciprocal of the overlap matrix $g_{\xi\gamma} = \langle \psi_{\xi} \mid \psi_{\gamma} \rangle$.

The conditions under which Equation 2.10 has to be solved is that at $t = -\infty$ it is in its entrance channel α, i.e. $c_{\beta}(-\infty) = \delta_{\alpha\beta}$.

The most important components in Equation 2.10 are the matrix elements $\langle \omega_{\beta}| \, V_{\gamma} - U_{\gamma} \, |\psi_{\gamma}\rangle$. These are the matrix elements mentioned above. They can be categorized into two: one for the inelastic excitation and the other for the exchange of nucleons between two partners.

For the inelastic excitation the radial part of the form factor can be written as the r-derivative of the potential

$$f_{\beta\gamma}^{inel}(r) = \beta_{\lambda}\frac{\partial U(r)}{\partial r} \, . \tag{2.11}$$

where β_λ is the deformation parameter that gives information on the collectivity of the state and U(r) is the average potential of entrance and of exit channels.

For the transfer process, in addition to the distance r between the two nuclei the form factor $f_{\beta\gamma}(\vec{\kappa}, r)$ depends also on the momentum transfer $\vec{\kappa}$. With the use of simple parametrization from Ref. [26] and at large distances the form factor can be written as

$$f_{\beta\gamma}^{tran}(0, r) \propto \frac{e^{-\kappa_{a_1'} r}}{\kappa_{a_1'} r} \ , \tag{2.12}$$

where coefficient $\kappa_{a_1'}$ contains the binding energy of the single particle state a_1' entering in the transition. This coefficient governs the asymptotic behaviour of the transfer form factor, which at large distances prevails over the nuclear component of the inelastic form factor.

2.2.2 Q-value dependence of the transfer probabilities

There is no need to solve explicitly the full system of coupled equations to estimate the magnitude of a given transfer process. Instead, it suffices to go through a first-order approximation. In this approximation, the probability of the transition from the entrance channel α to the channel β can be written in the form

$$P_{\beta\alpha} = |a_\beta^I(t)|^2$$

where the amplitude is given by

$$a_\beta^I(t) = -\frac{i}{\hbar} \int_{-\infty}^{t} \langle \psi_\beta | V_\alpha - U_\alpha | \psi_\alpha \rangle \ e^{i(E_\beta - E_\alpha)t'/\hbar} \ dt'$$

By approximating the true trajectory of the transferred particle with a parabolic parametrization around the turning point, the transition probability may be expressed as

$$P_{\beta\alpha} = \sqrt{\frac{1}{16\pi\hbar^2 |\ddot{r}_0| \kappa_{a_1'}}} \ |f_{\beta\alpha}(0, r_0)|^2 \ g(Q_{\beta\alpha}) \ , \tag{2.13}$$

where $\ddot{r}_0$ is the radial acceleration at the distance of closest approach r$_0$ for the

grazing partial waves. Thus, one can see that the probability for a given transfer is proportional to the square of the form factor times the adiabatic cut-off function that depends on the optimum Q-value of the reaction. The adiabatic cut-off function is given as

$$g(Q) = \exp\left[-\frac{(Q - Q_{opt})^2}{\hbar^2 \ \ddot{r}_0 \ \kappa_{a_1'}}\right] \tag{2.14}$$

where the reaction Q-value Q is defined as the difference between the final and the initial kinetic energy T of the recoils

$$Q = \Delta T = E_b + E_B - E_a \tag{2.15}$$

or more conveniently with the condition of momentum conservation [27]

$$Q = \frac{m_b + m_B}{2m_b m_B} \ p_b^2 - \frac{m_B - m_a}{m_B} \ E_a - \frac{\sqrt{2m_a E_a}}{m_B} \ p_b \cos\theta \tag{2.16}$$

where m_a, m_b and m_B are the masses of the projectile, of the ejectile and of the recoil, respectively, p_b is the momentum of the ejectile, E_a is the energy of the projectile, θ is the scattering angle.

The optimum Q-value Q_{opt} in Equation 2.14 is

$$Q_{opt} = \left(\frac{Z_d}{Z_A} - \frac{Z_d}{Z_b}\right) E_C + \left(\frac{m_d}{m_b} - \frac{m_d}{m_A}\right)(E - E_C) + \frac{m_d \ \ddot{r}_0}{m_a + m_A}(R_A m_b - R_a m_B) \tag{2.17}$$

where E_C is the Coulomb barrier and m_d and Z_d are the mass and charge of the transferred particle. From the first term in Equation 2.17 one can deduce that the optimum Q-value for neutron transfer is $Q_{opt} \sim 0$ and for proton transfer is $Q_{opt} \neq 0$.

The adiabatic cut-off function g(Q) defines the actual value of the transition probability whose maximum is at the optimum Q-value. For example, Figure 2.6 shows the the adiabatic cut-off function g(Q) for all one- and two-particle transfer channels for the reaction ^{58}Ni+^{208}Pb at 330 MeV. The location of all possible transitions is represented by the red lines. One can notice that there are cases when these red lines overlap with the Gaussian distributions meaning that the transfer channel is allowed. In our case, the allowed transfer channels are neutron pick-up
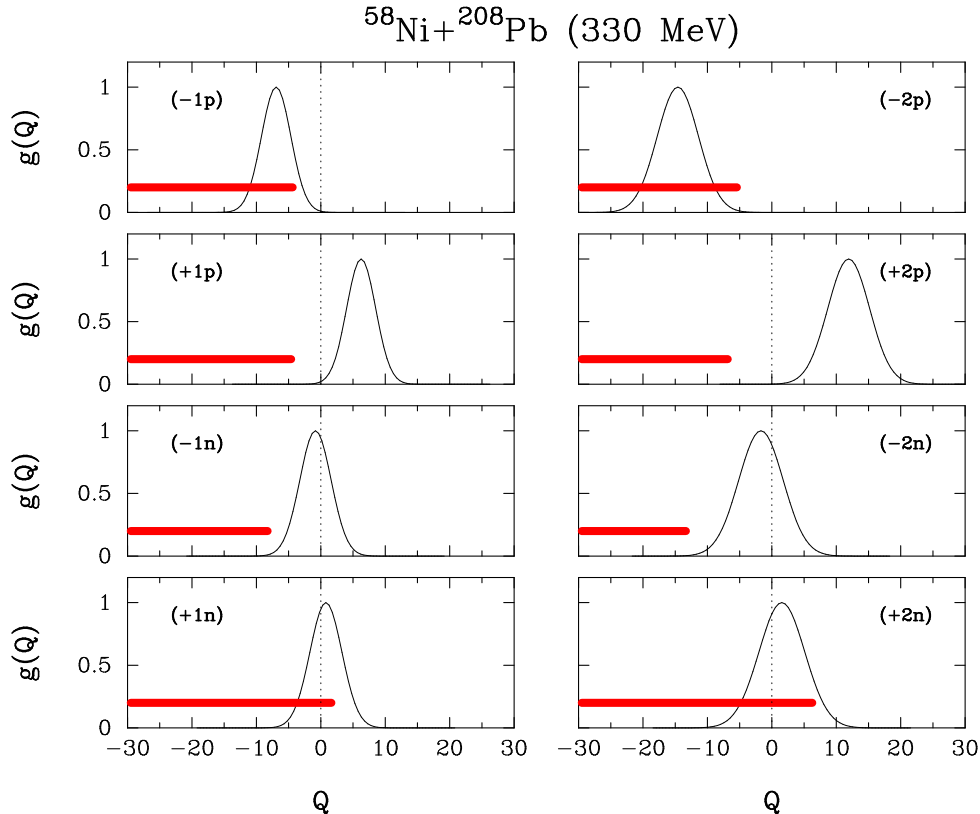
$$^{58}\text{Ni}+^{208}\text{Pb} \ (330 \ \text{MeV})$$

Figure 2.6: Adiabatic cut-off functions for one- and two-neutron and proton transfer channels for the reaction $^{58}\text{Ni}+^{208}\text{Pb}$ at 330 MeV. The Q-value is in MeV. The horizontal red lines represent the location of all possible transitions [10].

and proton-stripping. All the other channels are hindered by optimum Q-value consideration. The experimental proof of this behaviour can be found in Ref. [28]. It is also worth to note that for some channels, in particular two-proton stripping and two-neutron pick-up, the reaction mechanism favors transitions leading to high excitation energies.

It is required, for the optimum Q-value Q_{opt}, that the trajectories of the colliding nuclei match smoothly before and after the transfer process where the contribution of the form factor peaks.

2.2.3 The semi-classical GRAZING model

In the theoretical discussion of reactions between heavy ions it was shown that transfer processes can be treated within the semi-classical approach benifiting from the fact that the wavelength associated with the relative motion of the center of

mass of the colliding nuclei is much smaller than the interaction region [29]. This means that the trajectory of the ion can be approximated to be classical. Using this approximation the various semi-classical models have been successfully reproducing the experimental data. One of these kind of models is the GRAZING model, which was developed due to the necessity to have a description of MNT both in the quasi-elastic and the deep-inelastic regime [8, 10].

In the semi-classical model GRAZING, the interacting nuclei are described as an ensemble of independent nucleons that can vibrate around their spherical equilibrium shapes, the basic degrees of freedom being surface vibrations and single particle degrees of freedom. The two ions interact via a Coulomb plus nuclear interaction and can exchange nucleons. The Coulomb potential is represented by a two point charge expression, while the nuclear potential uses a Wood-Saxon parametrization. For excitation of the surface modes the macroscopic approximation whose form factors expressed in Equation 2.11 and whose strengths given by the experimental $B(E\lambda)$ is employed. For the exchange of nucleons instead the microscopic form factors taking into account the single-particle properties of the two colliding ions are used (see Equation 2.12). The different single-particle states participating to the transfer process are described by introducing average single particle level densities.

The GRAZING model have been successfully compared to a number of experimental data. As an example, the Figure 2.7 shows the comparison of the calculations performed by GRAZING model with the experimental total cross sections integrated by angle and Q-value for the various measurements of MNT at near barrier energies. One can notice that the model particularly well describes the data in the region of one-nucleon transfer channels, $(\pm 1p)$ and $(\pm 1n)$. Deviations between experimental data and calculations are more pronounced as more nucleons are transferred. The most probable explanation for this is that the GRAZING uses average level densities and calculates only direct component of the MNT reactions close to the grazing where the most of the cross sections from the quasi-elastic scattering are concentrated. The contributions leading to the deep-inelastic scattering are not fully considered.

The formalism used to construct the GRAZING model will be briefly described in Chapter 5.
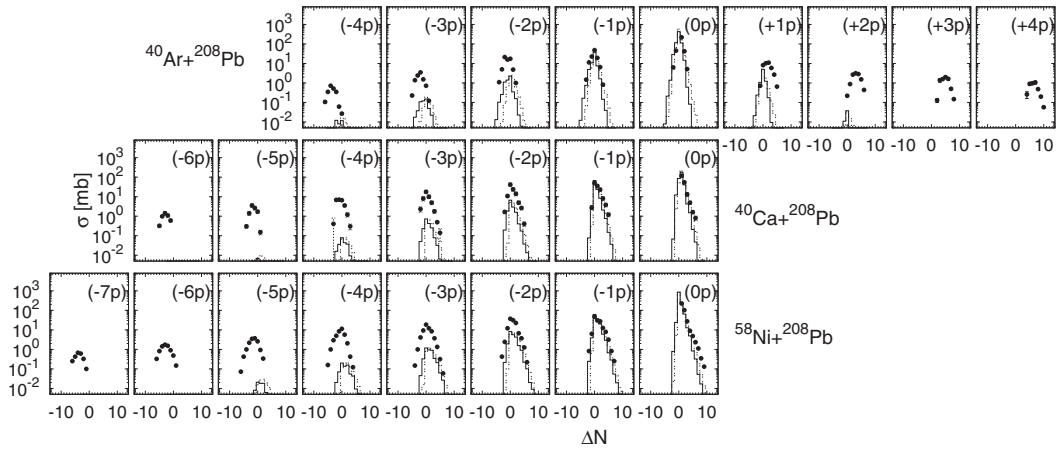
Figure 2.7: Total experimental cross section (angle and Q-value integrated) for the reactions of ^{40}Ar, ^{40}Ca, and ^{58}Ni induced on the ^{208}Pb target, at beam energies E_{lab}=6.4, 6.2 and 6 MeV/A, respectively (points) and the GRAZING calculations with (solid line) and without (dashed line) neutron evaporation [5].

Chapter 3

Experimental Setup

This chapter describes the experimental setup of the measurement of multinucleon transfer reactions of the ^{206}Pb+^{118}Sn system. First, the general view of the accelerator complex used in this experiment will be presented. Then it will continue with a discussion of the large solid angle magnetic spectrometers. Finally, a description of the PRISMA spectrometer including the various detectors will be reported.

3.1   Accelerators

All of the experimental work described in this thesis was conducted at the National Laboratories of Legnaro (LNL) [30]. The LNL are one of the four national laboratories of the Italian Institute of Nuclear Physics (INFN), where several available accelerators provide beams for nuclear and applied physics experiments. In this experiment, a ^{206}Pb beam was provided by the PIAVE-ALPI accelerator complex. The production of the ^{206}Pb at 1200 MeV was a very significant achievement since it is the heaviest beam ever accelerated at LNL.

PIAVE (Positive Ion Accelerator for Very-low Energy) is a positive ion injector for the linac ALPI [31, 32]. It operates at a frequency of 80 MHz with two Superconducting Radio Frequency Quadrupoles (SRFQ) followed by eight superconducting Quarter Wave Resonators (QWR). It has an equivalent voltage of about 8 MV which allows the acceleration of ions up to ^{238}U^{+28} from $\beta = 0.0089$ to $\beta = 0.045$ for an efficient injection into ALPI [11]. Figure 3.1 shows the layout of the PIAVE injector connected to the ECR ion source. The ECR (Electron Cyclotron Resonance) is a high voltage platform which generates the beams for the PIAVE.

ALPI (Acceleratore Lineare Per Ioni) is a linear accelerator. [12, 33]. It allows to boost the beams at energies ranging from 6 up to 20 MeV/A which is sufficient to

overcome Coulomb barrier of every beam-target system like, for example, the U-U [34]. Its operation is based on superconducting Quarter-Wave Resonators (QWR) in three different sections with different optimum velocities: a first low-β section with $\beta = 0.055$ (24 cavities) is followed by a medium-β section with $\beta = 0.11$ (44 cavities) which is followed by a high-β section with $\beta = 0.14$ (24 cavities) [35]. The cavities are cooled down by liquid helium to maintain them in a superconducting state. Figure 3.2 shows a sketch of the ALPI linac accelerator.

The accelerated beam is delivered to the experimental hall by means of the switching magnet which bends it on the beam line towards the dedicated experimental apparatus.

3.2 Large solid angle magnetic spectrometers

The magnetic spectrometers have been used for the spectroscopy of charged particles from the early days of nuclear physics. They have proven to be very powerful tools for the complete identification of the reaction products with the necessary ultimate resolution.

The role of the magnetic spectrometers in the transfer reaction studies is very important. The necessity to distinguish excited states populated in light ion transfer reactions lead to the development of magnetic spectrographs in the past. A combination of magnetic elements of different complexity, which focuses momenta at definite positions on the focal plane, allowed to achieve this goal. For example, the Q3D type spectrographs, consisting of one quadrupole focusing the ions to focal plane and three dipoles separating the ions with different p/q ratios, were employed for the one and two nucleon transfer studies. They are still used for the spectroscopic studies with an improved energy resolution up to 10 keV and the solid angles of few msr. The composed instruments require corrections for ion optical aberrations [10, 19].

In the reactions with heavier systems the transfer products have large energy dynamic range which requires larger acceptance of the magnetic spectrometer to have a sufficient detection efficiency by keeping a good resolution. The enlargement of the acceptance implies the use of complex magnetic elements. However, the required corrections for ion optical aberrations would make the detection system unfeasible. Therefore, the concept of trajectory reconstruction was applied instead by simplifying the magnetic element configuration. Combination of a simple magnetic configuration and tracking algorithms allows to reconstruct the trajectory
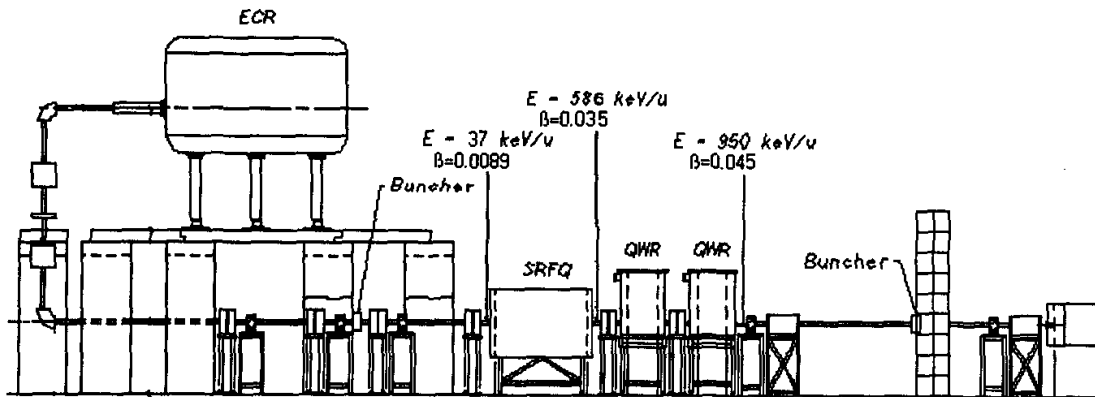
Figure 3.1: The layout of the PIAVE injector [11].
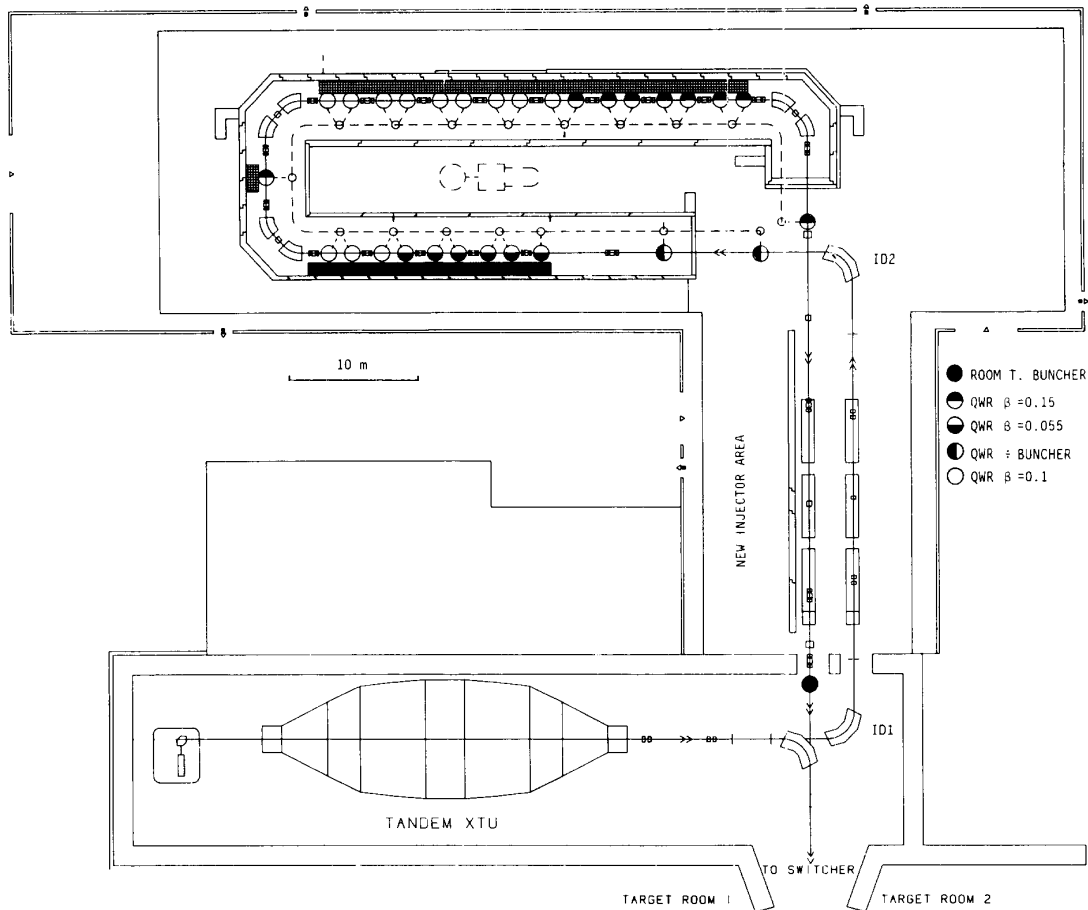
Figure 3.2: The layout of the ALPI linac (on the top) and the TANDEM (on the
bottom) accelerator [12].

of the ions. In this way, the new generation of magnetic spectrometers such as PRISMA [36] , VAMOS [37, 38] and MAGNEX [39] with solid angle up to 100 msr are obtained. They are successfully used for a complete identification of the transfer products providing their nuclear charge, mass, Q-value and their associated cross sections.

3.3 The PRISMA spectrometer

PRISMA is a large acceptance magnetic spectrometer designed for the identification of the reaction fragments of heavy-ion collisions in the energy range of 5–10 MeV/A. A picture of PRISMA is shown in Figure 3.3. The spectrometer is mounted on a platform that can be rotated around the target point in the angular range of -20° $\leq \theta \leq +130°$ with respect to the beam direction which makes two-body reactions (such as multi-nucleon transfer) possible to study. It has following components:

- two optical elements:
  - a quadrupole magnet
  - a dipole magnet
- a detection system providing information on the position, the time of flight (TOF) and energy:
  - a Micro-Channel Plate (MCP) entrance detector
  - a Multi-Wire Parallel Plate Avalanche Counter focal plane detector (MW-PPAC)
  - an Ionization Chamber (IC).

The sketch of the optical design is shown in Figure 3.4. The MCP start detector and the MWPPAC focal plane detector measure the position of the incoming ions (in x and y) and provide the time of flight. The intrinsic time resolution of the start and stop detectors are about 300-400 ps. This together with the long time of flight distance ($\sim$6m) makes an overall good time of flight resolution. The ionization chamber is a ΔE-E telescope detector used to identify the atomic number of the reaction products. The software algorithms based on an event-by-event reconstruction of the ion trajectory allows to obtain the mass of the ion by combining the information coming from the different detectors of the spectrometer. The main features of PRISMA are summarized in Table 3.1.

Table 3.1: The characteristics of the PRISMA spectrometer [19].

Solid angle Ω	80 msr
Mass resolution	1/300 (Via TOF)
Nuclear charge resolution	1/60
Energy resolution	1/1000 (via TOF)
Momentum acceptance	$\pm$ 10%
Maximum Bρ	1.2 Tm
Angular acceptance	$\Delta\theta$= 12° and $\Delta\phi$=22°
Count rate capability	100 kHz
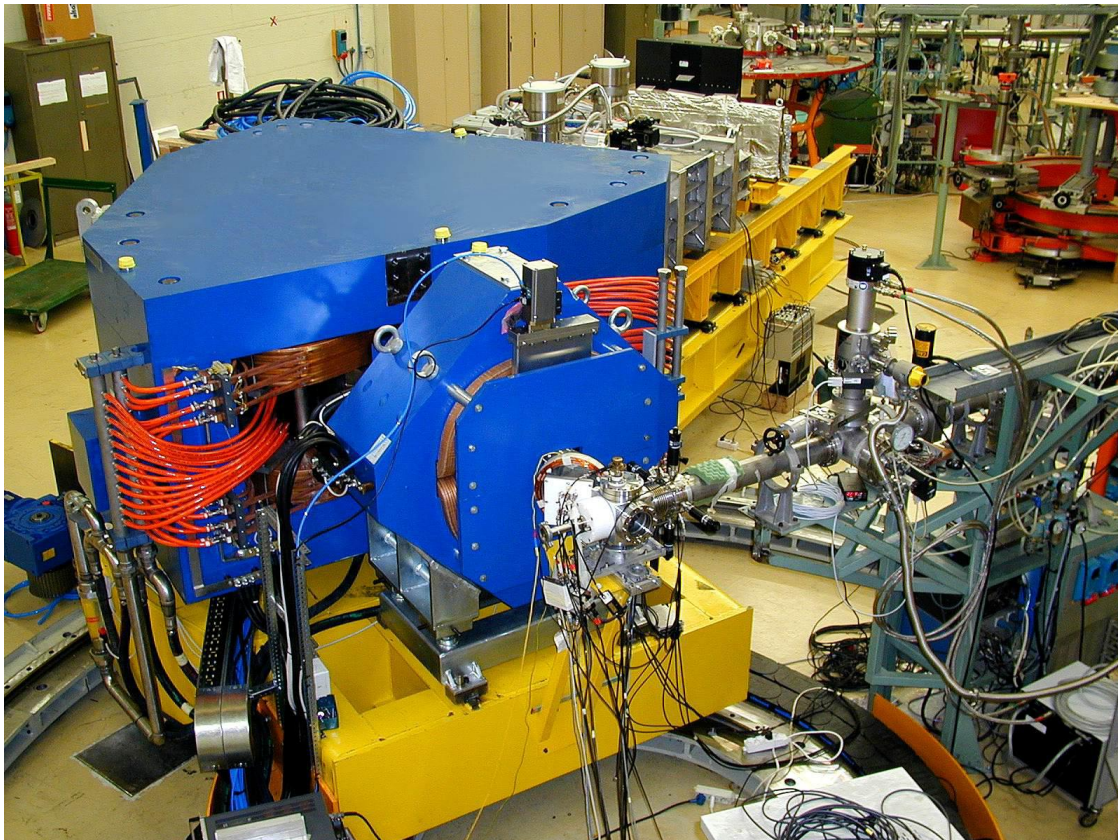
Figure 3.3: The PRISMA spectrometer [13].
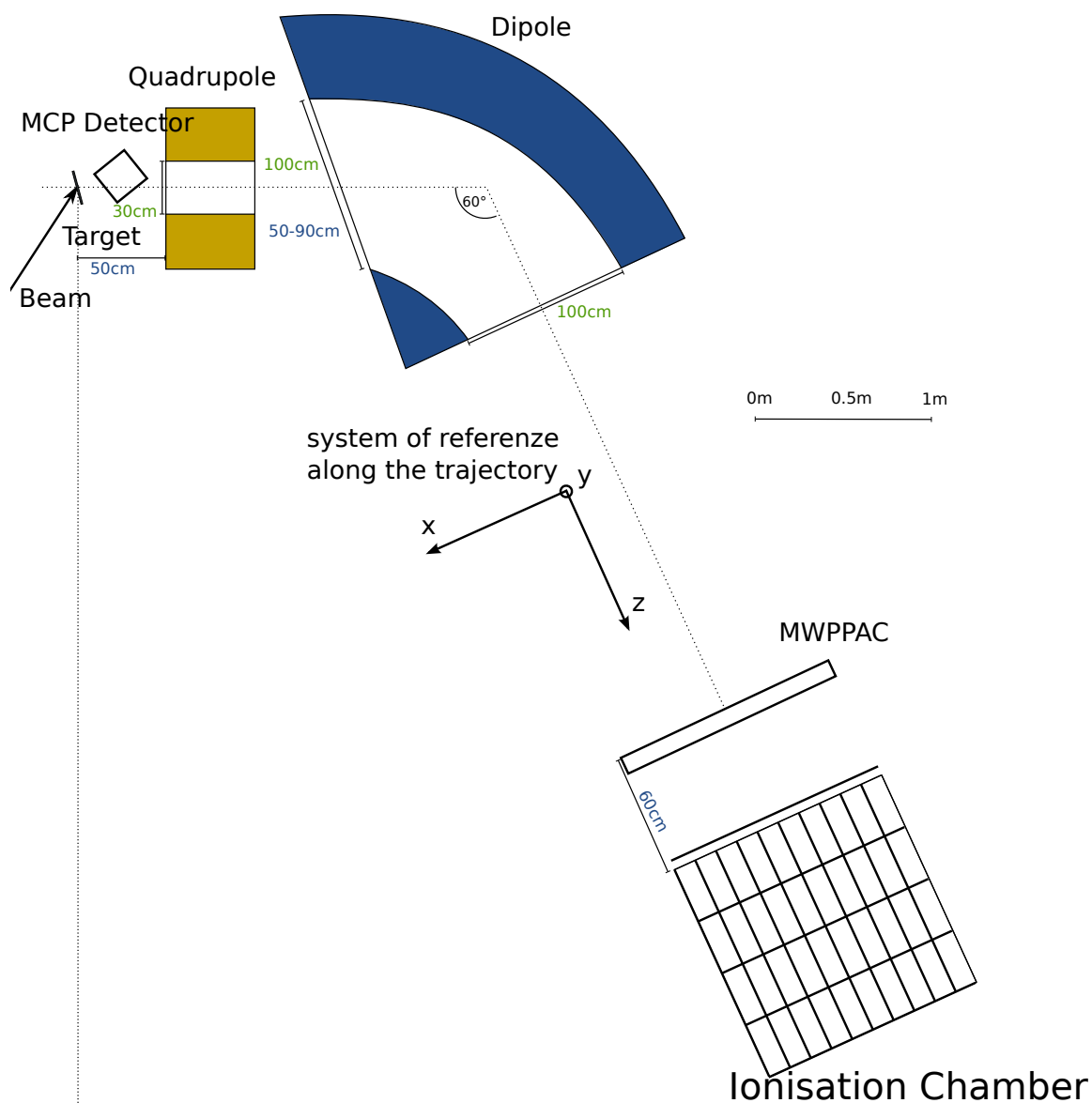
Figure 3.4: Schematic layout of the PRISMA spectrometer. Labels represent the distance between components (blue) and the diameter of the beam tube (green) [14].

3.3.1 Microchannel Plate Detector

The ions entering the PRISMA spectrometer are detected by the Micro-Channel Plate detector (MCP) [15]. It defines the whole solid angle of PRISMA with a detecting surface of 80×100 mm² at a distance of 25 cm from the target (thanks to the high counting rate capability of MCP allowing to mount the detector in such a close distance to the target position). The detector is placed at an angle of 135° with respect to the optical axis of the spectrometer. Figure 3.5 shows a schematic layout and a picture of the MCP detector (as it viewed from the target).

The entrance detector provides the position information of the reaction fragments in X and Y directions with a spatial resolution of 1 mm which corresponds to an angular resolution of less than 0.5°, and a timing signal for the time of flight measurements between entrance and focal plane detectors of PRISMA with a time resolution of around 350 ps and efficiency close to 100% for heavy ions at a few MeV/nucleon.

The incoming ions pass a thin self-supporting carbon foil of 20 μg/cm². The backward emitted electrons, induced by the ions, are accelerated by an electric field and a parallel magnetic field to preserve the position information on their way to the MCP. Two rectangular Micro-Channel Plates mounted in the Chevron configuration amplify the signal by multiplying the electrons. The produced charge is collected by the position-sensitive anode made of two ortogonal delay lines (horizontal and vertical). The position information is obtained from the difference in arrival time of the signals. This fast timing signal is also used for the time of flight measurements
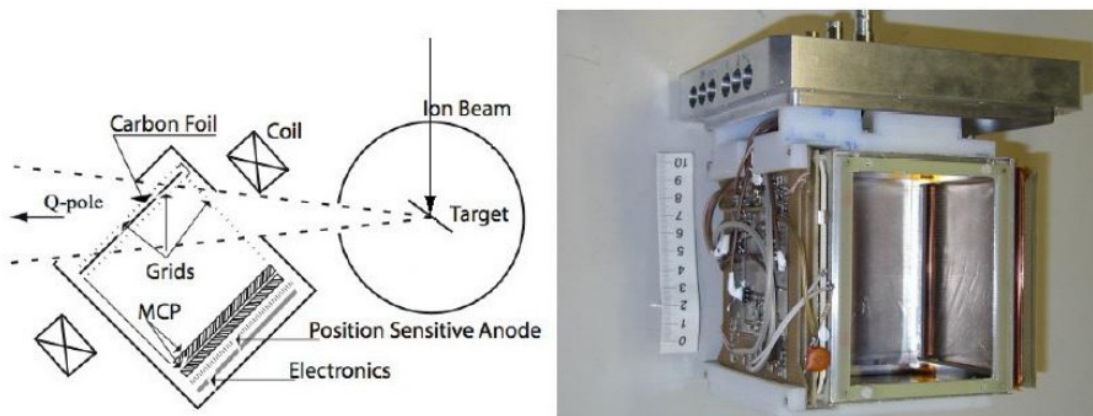
Figure 3.5: A schematic view (left) and a picture (right) of the MCP entrance detector [15].

of the MCP and the MWPPAC.

3.3.2 Ion Optical Elements

After the MCP, the beam-like fragments go into the optical system which has two magnetic lenses: a quadrupole and a dipole. The former focuses the incoming ions on the vertical axis and disperse on the other while the latter bends the trajectory of the ions travelling to the focal plane detectors. In this way, the trajectory of the ions within the spectrometer are determined by taking into account the entrance and the exit position.

Quadrupole The quadrupole singlet is located at a distance of 50 cm away from the target position. It has a length of 50 cm and a aperture diameter of 30 cm. This magnet focuses in the vertical (Y) direction and defocuses in the horizontal (X) direction.

Dipole The dipole singlet follows the quadrupole singlet at a distance of 60 cm. It has a bending angle of 60° with a curvature radius of 1.2 m. It is manufactured to have a homogeneous field in the 1 m wide beam pipe with a maximum magnetic field of 1 T which corresponds to a maximum rigidity of $B\rho = 1.2$ Tm. This magnet bends the ions to the different positions in the focal plane detectors according to their magnetic rigidity.

To simplify analysis procedure the ion trajectories are supposed to be straight lines in the region from the quadrupole to the dipole and after exiting the dipole since they are not affected by any magnetic field.

The fringing fields are small enough compared to the inner field of magnets since the dipole's longitudinal dimension is large compared with the transversal one. This guarantees the planarity of the trajectory.
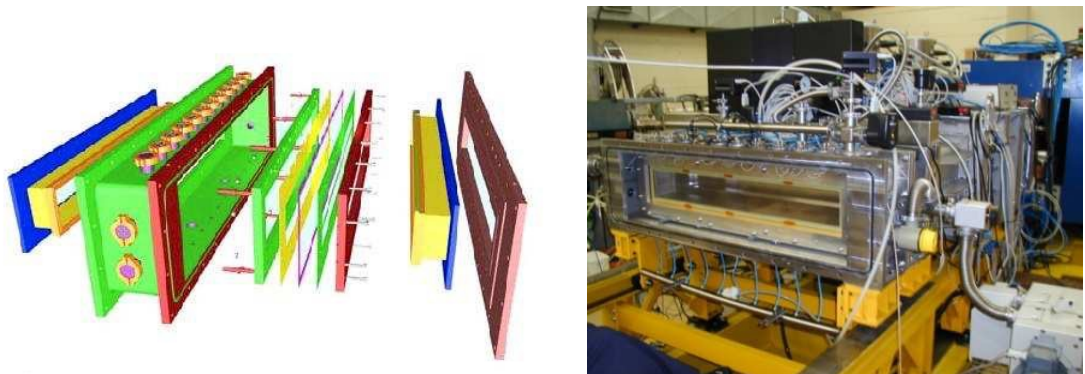
Figure 3.6: A schematic layout (left) and a picture (right) of MWPPAC [16].

3.3.3 Multiwire Proportional Plate Avalanche Counter

The ions exiting the dipole after 3.2 m drift in vacuum are detected by the Multiwire Proportional Plate Avalanche Counter (MWPPAC) [16]. It consists of 10 equal sections, with a beam-facing surface of 10×13 cm^2 each, covering a total area of 100×13 cm^2 in order to match the large acceptance of the spectrometer. Figure 3.6 shows the exploded view and a picture of the MWPPAC.

The MWPPAC detector provides the focal plane position of the ions along the x axis and the y axis having a position resolution of 1 mm and 2 mm, respectively. Besides the position information, it provides a timing signal for both the time-of-flight (TOF) measurements between the MCP and the MWPPAC, and Data Acquisition trigger. The calculation of the TOF is important because of the trajectory reconstruction procedure. It reaches the time resolution of about 300 ps and the efficiency of around 80% for heavy ions at energies a few MeV/nucleon [18].

Each section of the detector has a three electrode structure: two orthogonal anode wire planes to determine the horizontal and vertical positions, and a central cathode placed 2.4 mm downstream and used for timing. The 100 anode wires in each pad are placed in steps of 1 mm on the horizontal axis whereas on the vertical axis the wires are connected in groups of two covering the entire length of the detector with a step of 1 mm. The position signals are obtained by means of the delay lines from each side of the section: left and right. The relative delay is proportional to the position of the ion. The avalanche of the secondary electrons created by the ion
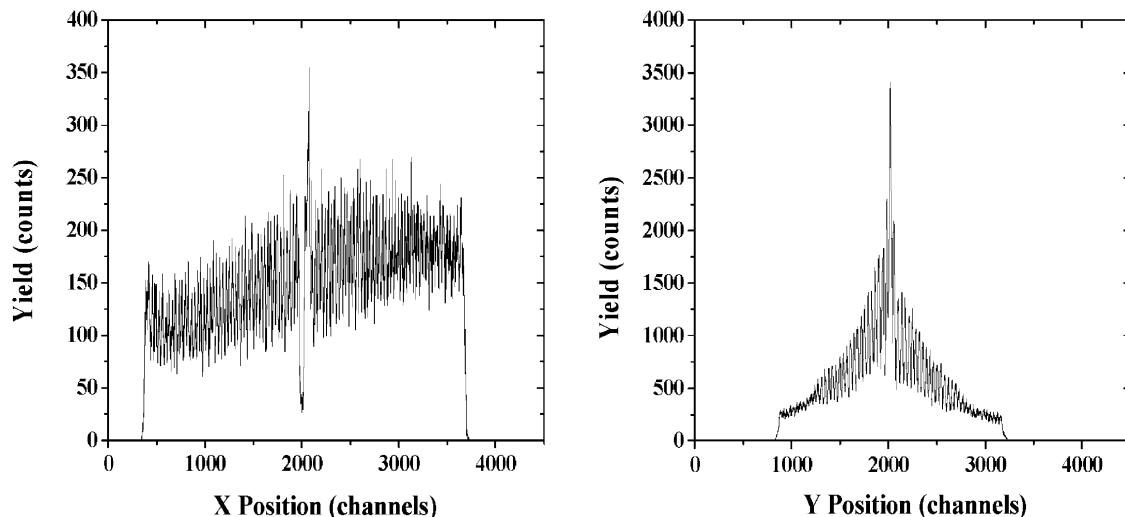
Figure 3.7: Typical position spectra of one section of the MWPPAC in X (left) and Y (right)[16].
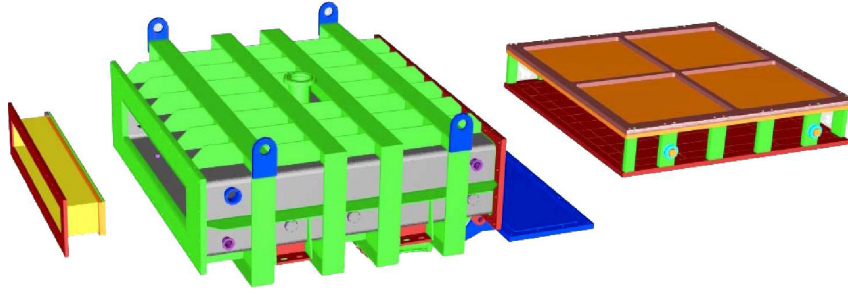
Figure 3.8: Schematic view of the IC [16].

is well localized since each wire is an independent counter (typically only one wire is firing). Figure 3.7 shows the typical X and Y position spectra of one section of MWPPAC. The cathode is polarized at negative potential in range of 500-600 V and the anode placed at ground potential. The detector operates with isobutane gas (C_4H_{10}) at working pressures of 7-8 mbar.

3.3.4   Ionization chamber

The focal plane MWPPAC detector is followed by an Ionization Chamber (IC) at a distance of 60 cm [16]. It has dimensions of $110(X) \times 20(Y) cm^2$ to match the large acceptance of the spectrometer and an active depth (Z) of 120 cm. Such a long depth was chosen due to the stopping power and the maximum pressure of the used gases which make the path length of heavy ions comparable with this depth. Figure 3.8 shows the exploded view of the IC.

The IC allows to measure the total energy of the ions and their energy loss in the gas. Combining the information on the total energy and the energy loss of the ions one can obtain the atomic number Z of the ion, see Figure 3.9. An energy resolution of 1-2 MeV has been achieved for a medium-mass ions at few MeV/A even for such large dimensions of the detector [19].

The IC is divided into 40 sections: 10 sections on the horizontal axis and 4 sections along straight trajectories. Each of them has dimensions of 25×10 cm^2 measuring the energy loss ΔE and the total energy E. In each section, the energy loss is obtained by measuring the number of electron-ion pairs created by direct ionization in the gas by applying electric fields [40]. By summing the energy loss in all sections one can obtain the total kinetic energy of the fragment.

The IC consists of anode pads, a common cathode and a common Frisch grid. The use of the Frisch grid makes sure that the amplitude of the signal is independent of the entrance position of the ion. Figure 3.10 shows the inner view of the IC.
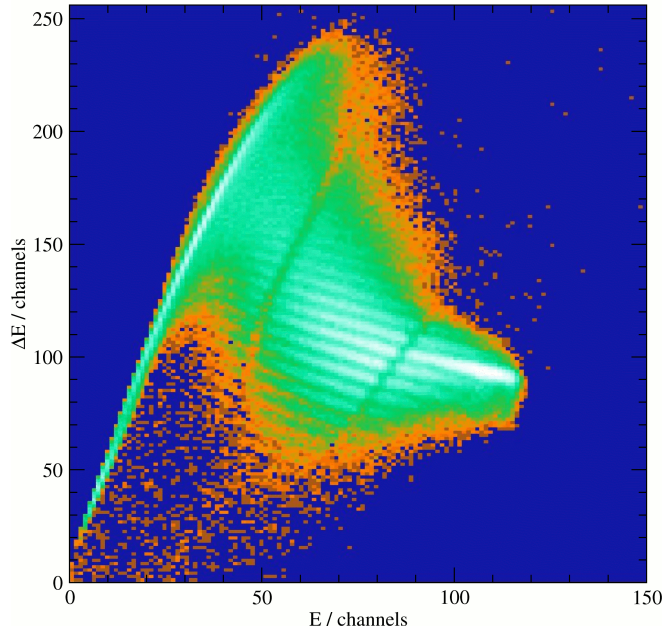
Figure 3.9: Example of ΔE-E matrix for the ^{82}Se + ^{238}U reaction at E_{lab} = 505 MeV [13]. The most intense line corresponds to the ^{82}Se (Z=34).

The detector usually operates with methane (CH_4) and carbon-tetrafluoride (CF_4), due to the high electron drift velocity, which allows to preserve good energy resolution even with the high counting rates needed in the experiments. In our case, the CF_4 was used due to its higher stopping power for high energy ions.

Additional 8 side detectors are placed on the left (4 detectors) and on the right (4 detectors) for veto purposes eliminating the ions with highly distorted trajectories.

Figure 3.10: Inner view of the IC [16].

Chapter 4

Data analysis

This chapter presents the analysis of data collected from the PRISMA spectrometer described in the previous chapter. PRISMA was employed in the ^{206}Pb+^{118}Sn experiment performed in inverse kinematics.

First, the details on the experiment including the position of PRISMA will be presented. Then the calibration procedure of the various detectors consisting in the spectrometer will described. Finally, the yield of each nuclear charge produced in the present experiment will be determined.

4.1 ^{206}Pb + ^{118}Sn experiment

The experiment of multinucleon transfer reaction was performed by using a ^{206}Pb beam with average currents of $\sim$2 pnA delivered by the superconducting PIAVE-ALPI accelerator complex of LNL, impinging onto a 200 μg/cm^2 strip ($\sim$2 mm) ^{118}Sn target with a purity of 99.81%. The Sn material was sandwiched between two 15 μg/cm^2 C films in order to reduce the sputtering process on the target surfaces. The measurement of an excitation function was performed at three different bombarding energies, E$_{\text{lab}}$=1200, 1100 and 1035 MeV, see Figure 4.1. For the highest energy PRISMA was positioned close to the grazing angle at θ_{lab}=35° and then at θ_{lab}=25°. At two lower energies the angle of PRISMA was kept fixed at θ_{lab}=25° since below the Coulomb barrier (E$_{\text{lab}}\sim$1041 MeV) the maximum of angular distributions of transfer flux was at forward angles in the laboratory frame (backward angles in the center of mass frame). In this way, the target-like ions had sufficient kinetic energies to be registered with good resolution, also at low beam energy, see Figure 4.2. The kinematics of the reaction allows also part of the beam-like ions to enter the spectrometer, being the limiting angle for Pb close to θ_{lab}=35°. The magnetic fields

and the gas pressures within PRISMA to detect and completely stop the reaction products of the present experiment are summarized in Table 4.1.

$$^{206}Pb + {}^{118}Sn$$
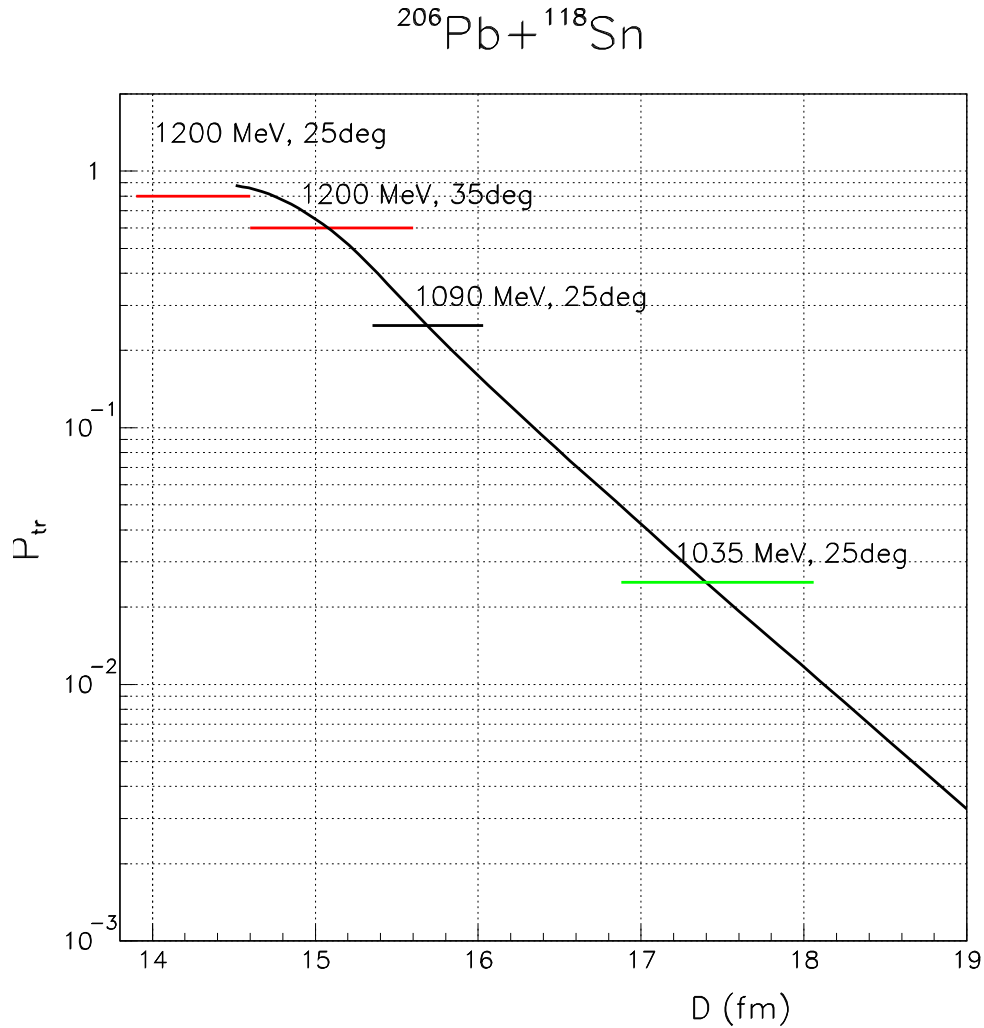
Figure 4.1: Transfer probabilities as a function of the distance of closest approach D for neutron transfer channels calculated by Grazing code. The colored lines indicate the region of D covered by PRISMA at the corresponding nominal bombarding energies and the angles of PRISMA. [17]. With these settings (from top to bottom) the measurements were performed.

The Figure 4.1 shows how the experiment evolved. An excitation function from above to well below the Coulomb barrier was measured by varying the beam energy from 1200 to 1035 MeV. Among these three energies, the highest energy is the one where one can have the highest kinetic energy of the reaction fragments and the highest cross section for the transfer channels, in particular for the proton transfer
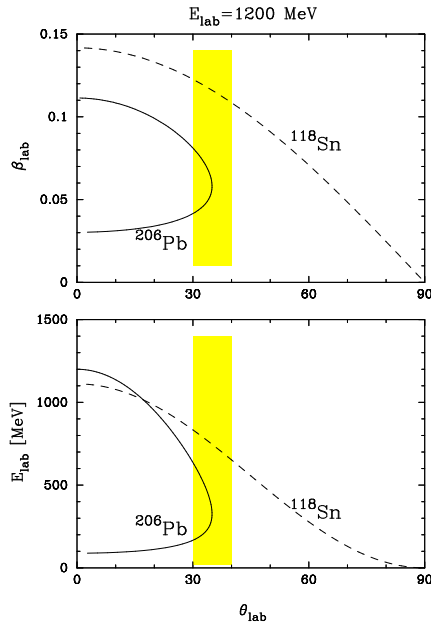
Figure 4.2: Kinematics of the ^{206}Pb+^{118}Sn reaction at E_{lab}=1200 MeV. The shaded (yellow) region corresponds to the PRISMA acceptance at θ_{lab}=35° [9].

channels. Therefore, the focus of this thesis is to identify nuclear charge of the transfer products in the region of Sn-like ions at the highest bombarding energy at both angles so to get the best resolution in the IC.

In addition, two silicon detectors were mounted in the sealed chamber. These detectors were used as monitor detectors during the experiment to get pure Rutherford scattered ^{118}Sn ions, to normalize the measured angular distributions, to get information on the beam position and the target thickness. The monitors were placed at θ_{lab}=48° and θ_{lab}=58° when the angle of PRISMA was set to θ_{lab}=35°, and then the angles of Si detectors were changed to θ_{lab}=58° and θ_{lab}=68° for the PRISMA placed at θ_{lab}=25°.

Table 4.1: PRISMA settings. For E_{lab}=1200 MeV.

Detection angle	35°	25°
Dipole field strength	0.867 T	0.921 T
Quadrupole field strength	0.798 T	0.852 T
MWPPAC fill gas	C_4H_{10} at 6 mbar	
IC fill gas	CF_4 at 34.5 mbar	

4.2 Presorting of the data

The PRISMA spectrometer deflects ions according to their momentum and charge, and provides their atomic number, atomic charge state, mass and velocity. The identification of the atomic number, which is the main objective of this thesis, is done by using the energy loss of the ions as a function of the total energy released in the ionization chamber.

The analysis procedure serves as a basis for future analysis of complete identification which includes the atomic mass, Q-value, etc. The atomic mass number can be obtained via an event-by-event reconstruction of the ion trajectory inside the magnetic elements of PRISMA, making use of time of flight and position information at the entrance and at the focal plane of the spectrometer. Therefore, to extract the relevant physical information a careful calibration of the entrance and of the focal plane detectors of PRISMA is necessary. A description of the calibration procedure applied to each detector will be given in the subsections below.

4.2.1 The Entrance Detector (MCP)

Being the first detector of the spectrometer, MCP provides the first interaction point (x, y) of the incoming ion. The x and y raw positions measured by the MCP are shown in Figure 4.3 (left).

Two lines and the cross are clearly visible. The lines are the shadows of nails which were put inside the quadrupole and the cross is the shadow of the metallic cross-shaped mask. The metallic mask is mounted at about 1 cm upstream of the
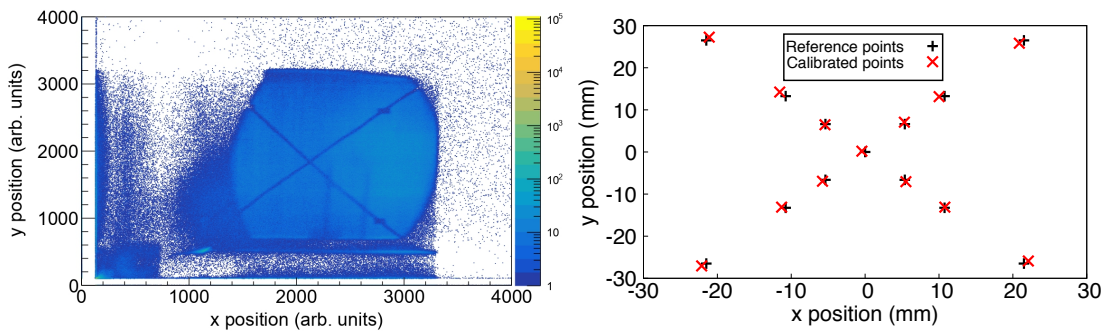
Figure 4.3: The raw data (left) in x and y coordinates of the MCP detector and calibration plot of the raw data with respect to the reference points (right). The random events were eliminated by putting a polygonal gate on the spectrum.

Table 4.2: Reference positions of the cross installed to calibrate the MCP detector.

	position x (mm)	position y (mm)
centre	0	0
top left	-21.5	26.5
top right	21.5	26.5
bottom left	-21.5	26.5
bottom right	21.5	26.5

carbon foil. It has 5 reference points used to calibrate the x and y positions of the MCP, see Table 4.2 .

Before the calibration of the x and y signals one should take into account that the mounted mask is usually rotated of about 2-3° during the experiment. In order to rotate and stretch the raw coordinates it is necessary to correct the two lines, mentioned above, making them vertical again. This is achieved by means of the coefficient matrix, with the diagonal elements equal to 1, multiplied by the raw data:

$$\begin{pmatrix} x^{'} \\ y^{'} \end{pmatrix} = \begin{pmatrix} 1 & a \\ b & 1 \end{pmatrix} \begin{pmatrix} x_{raw} \\ y_{raw} \end{pmatrix}$$

Then the transformed coordinates are calibrated from channels to millimeters using a cubic polynomial (x) or a linear polynomial (y):

$$x_{cal} = A_x + B_x x^{'} + C_x x^{'2}$$

$$y_{cal} = A_y + B_y y^{'}$$

Figure 4.3 (right) shows the calibration procedure. One can notice that the number of reference points in the plot are more than the number of points given in Table 4.2. This is due to the fact that there are more parameters than reference points for the fit. Therefore, to improve the fit, additional points in between the center of the cross and the other reference points were used. The parameters of the calibration proce-
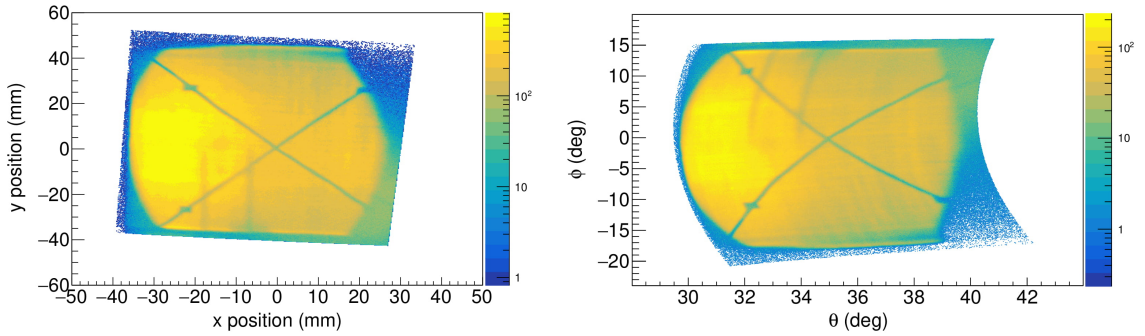
Figure 4.4: Calibrated spectra of the MCP detector in carthesian (left) and polar (right) coordinates.

dure are obtained by a least-square fit of the distance between the calibrated points and the reference points; and the outcome of the calibration is quite satisfactory.

Figure 4.4 shows the calibrated MCP plane in carthesian and in polar coordinates. The spectra were transformed into polar coordinates according to the equations in Appendix A of Ref. [41]

To eliminate noise contributions a gate on the MCP was set.

4.2.2 The Focal Plane Detector (MWPPAC)

As it was already mentioned in Section 3.3.3 the MWPPAC consist of 10 sections, see Figure 4.9. Each section provides 5 signals:

- x_R: horizontal right position

- x_L: horizontal left position

- x_C: cathode signal

- y_R: vertical right position

- y_L: vertical left position

Among these signals, the first 3 are of interest, because they are used to determine the focal plane position x_{fp} of the ions which allows to reconstruct their trajectory while the last two have less effect on the trajectory reconstruction and are mainly used to check the centering of the beam. The signal from cathode x_C is also used to measure the Time Of Flight (TOF) of the detected ions between the MCP and the MWPPAC detectors by means of a Time to Amplitude Converter (TAC).

The signals from horizontal right x_R and left x_L positions are propagating by means of the delay lines. So by subtracting them one can obtain the focal plane position x_{fp} of the ions in each section:

$$x_{fp} = x_R - x_L \tag{4.1}$$

But the use of delay line method and the limited efficiency of the MWPPAC may result in one of the two horizontal position signals missing (x_R or x_L). In order to recover the missing signal the cathode signal is used since its amplitude must be the same as the sum of two horizontal signals:

$$x_C = x_R + x_L \tag{4.2}$$

Figure 4.5 (left) shows how the relation above allows to select "good" events and to reduce the "noise" contribution by putting a polygonal gate on the matrix $x_R + x_L$ versus x_C. The ideal case, according to Equation 4.2, would be to get a point-like structure with no missing signals. For us this is not a case as it can be seen in Figure 4.5 (left) showing the vertical line where sum of left and right signals is lower than the cathode signal. The missing events are recovered by substituting the missing signal by the cathode signal. If the right signal is missing, then Equation 4.1 becomes x_C - x_L while for the left missing signal it becomes x_R - x_C. Figure 4.5 (right) shows the recovery procedure of the missing left signal which incorporates the bidimensional plot of $x_{fp} = x_R$ - x_L versus x_R - x_C. The obtained offset and the
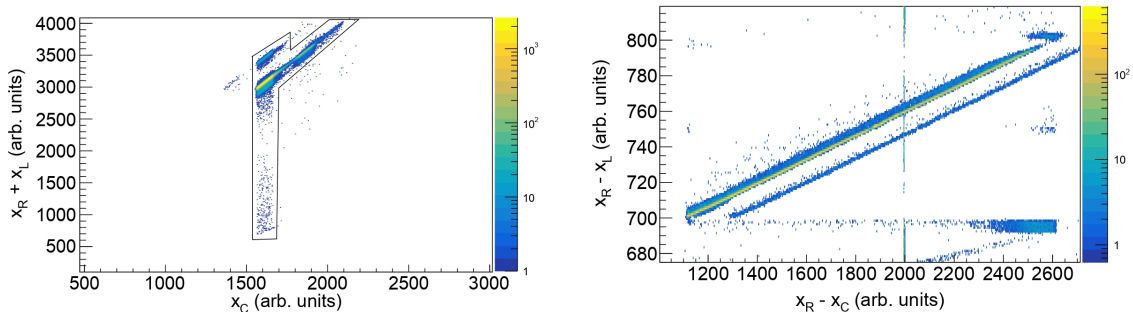
Figure 4.5: A polygonal gate to suppress the background signals on one of the sections of MWPPAC (left) and the recovery procedure of a missing signal (right).
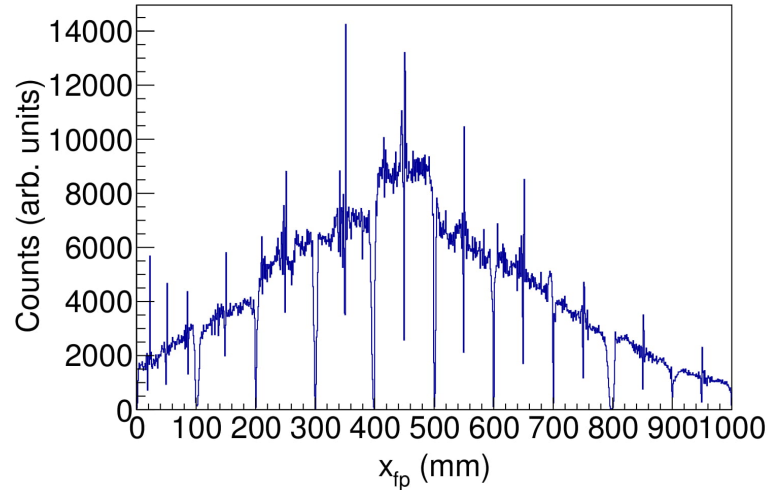
Figure 4.6: The calibrated focal plane position x_{fp} of the detected ions.

slope of the calibration curve corresponding to each section were used to reconstruct the position of the incomplete events. The missing right signal was recovered in a similar way.

Summing the position information from all 10 sections and then calibrating them into millimeters with a first-order polynomial the focal plane position x_{fp} was obtained. Figure 4.6 shows the final spectrum of the x position of the detected ions in the focal plane. One can notice the spacing each 100 mm and the central channels of each section having more statistics than the other. The spacing is due to the separation between the different sections of the MWPPAC. The higher amount of counts in central channels in each section is the result of the two short-circuited central wires in each section of MWPPAC which is done for the calibration purposes.

The Time of flight (TOF)

In order to identify the mass and the charge state of the reaction fragments it is necessary to measure their time of flight (TOF) through the spectrometer as it is governed by the equation

$$\frac{A}{q} = \frac{B\rho}{L} \, TOF \qquad (4.3)$$

where A/q is the mass-over-charge ratio, $B\rho$ is the magnetic rigidity (which includes the magnetic strength B of the dipole and the curvature radius ρ of the trajectory)

Table 4.3: TOF of the elastically scattered Sn-like ions. For E_{lab}=1200 MeV.

Detection angle	25°	35°
L (m)	$\simeq 5.9$	
v (cm/ns)	3.83	3.44
TOF (ns)	155.5	171.4

and L is the path length of the trajectory. L and ρ are calculated by PRISMA manager routines used to reconstruct the path of the ions.

The TOF is measured with ten Time to Amplitude Converters (TAC) using the signals of the MWPPAC sections as a start and the delyed MCP signal as a stop so to reduce the dead time from the TAC. Later ten output signals are calibrated from ADC values into ns by means of the calibration coefficients provided by the local team. The TOFs of ten sections are not initially aligned with respect to each other. Therefore the alignment procedure of different sections is performed. Then to obtain the velocities of the reaction products it was necessary to set a common TOF offset. The tuning of the TOF offset with a good precision is usually done by using the gamma spectra measured by AGATA (or CLARA) in coincidence with the ion detected by PRISMA. However, no coincidence measurement was performed in this experiment, therefore one had to calculate the TOF of the elastically scattered Sn-like ions through the PRISMA spectrometer so to use it as a reference for the common TOF offset. The velocities of the elastically scattered Sn-like ions (v) for both PRISMA angles (25° and 35°), the length of the trajectory in PRISMA (L) and the calculated TOFs ($TOF = L/v$) are given in Table 4.3.

The aligned and calibrated spectrum of the TOF versus x_{fp} for the ^{206}Pb+^{118}Sn reaction measured by PRISMA at 35° is shown in Figure 4.7. One can see the diagonal lines corresponding to the different mass-over-charge ratio of the reaction products.

Figure 4.8 shows the TOF and β spectra of the ions detected at 35° of PRISMA. It is interesting to note that among two reaction partners only Sn-like ions can be clearly distinguished. This is due to the reaction kinematics which have a limiting angle for Pb close to θ_{lab}=35° allowing part of the Pb-like ions to be accepted by the spectrometer, see Figure 4.2.

Similar procedure involving alignment and calibration of TOF versus x_{fp} spectrum was applied for the measurement at 25° of PRISMA.
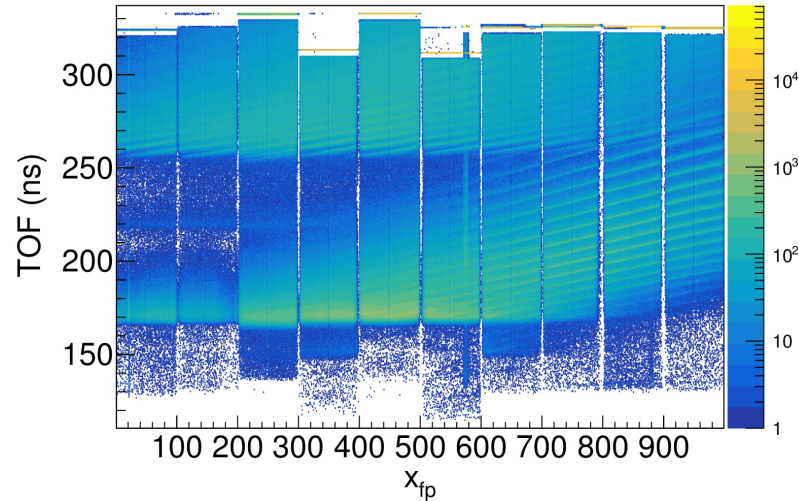
Figure 4.7: The final spectrum of the TOF versus the horizontal position on the focal plane x_{fp} for the measurement at 35° of PRISMA.
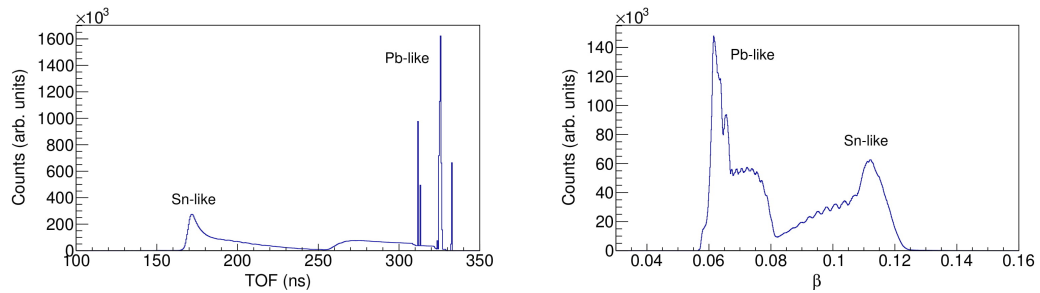
Figure 4.8: TOF (right) and β (left) distributions for PRISMA measured at 35°. The title referring to the Pb-like ions is for the illustration purpose only. The pedestal coming from the electronics in this region is clearly visible instead.

In our analysis the region of interest in the spectrum was the Sn-like ions and it was important to reduce the contribution of the Pb-like ions to this region. This goal was achieved by means of the determined TOF of the ions which reduced the contribution of the Pb-like ions significantly.

4.2.3 The Ionization Chamber (IC)

Being the last detector of the spectrometer, the IC fully stops the incident particle and provides its atomic number with ΔE-E method, see Section 4.3.

As already discussed in Section 3.3.4, the IC consist of 40 sections. Each section measures the energy loss of the passing fragment independently and therefore all

40 sections need a proper calibration. The calibration is usually done before the experiment using the gain coefficients obtained by means of a pulser which sends signals in each section of the IC. Thus, one can match the gains of the different sections. This gain matching procedure does not give energy values in MeV but does the alignment of the signals in each section only. Figure 4.10 shows the raw spectra of the ions produced in ^{206}Pb+^{118}Sn reaction depositing their energy within the 4 sections that compose one of the central rows of the IC. One can see the red lines referring to the lower and upper thresholds relative to each section. The lower threshold was set in order to eliminate the pedestal at the beginning of the spectrum. The upper threshold was applied to get rid of noise in the last channels of the IC.

Figure 4.9 shows the IC and the MWPPAC in combination with the different scenarios for the ion trajectories. It is common to both of them that only those ions reaching the IC are considered during offline analysis. Among them, the ions with highly distorted trajectories firing in one of the side pads, placed on both sides of the
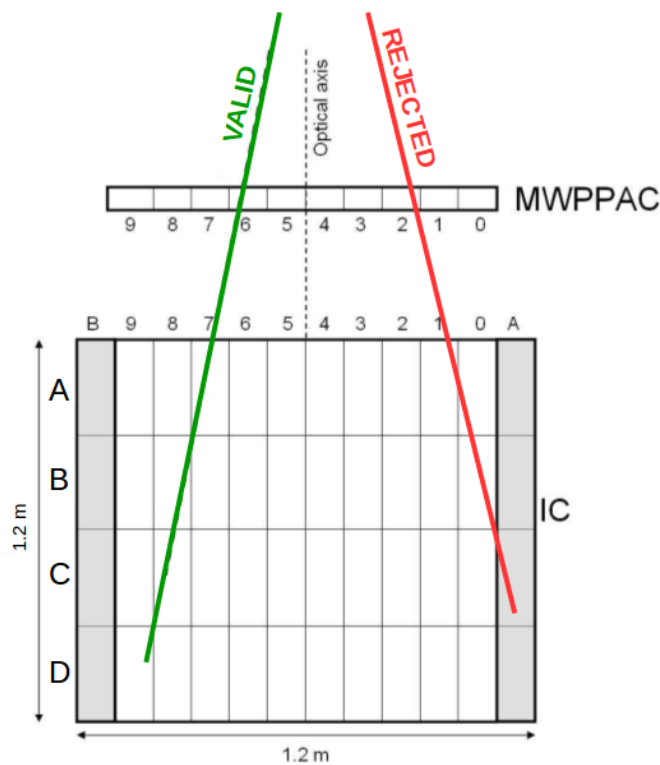
Figure 4.9: The layout of the Focal Plane Detectors (FPD) including the MW-PPAC and the IC. The side pads of the IC are in grey. The three different examples of the ion trajectories within the FPD are drawn (see text for details) [18].
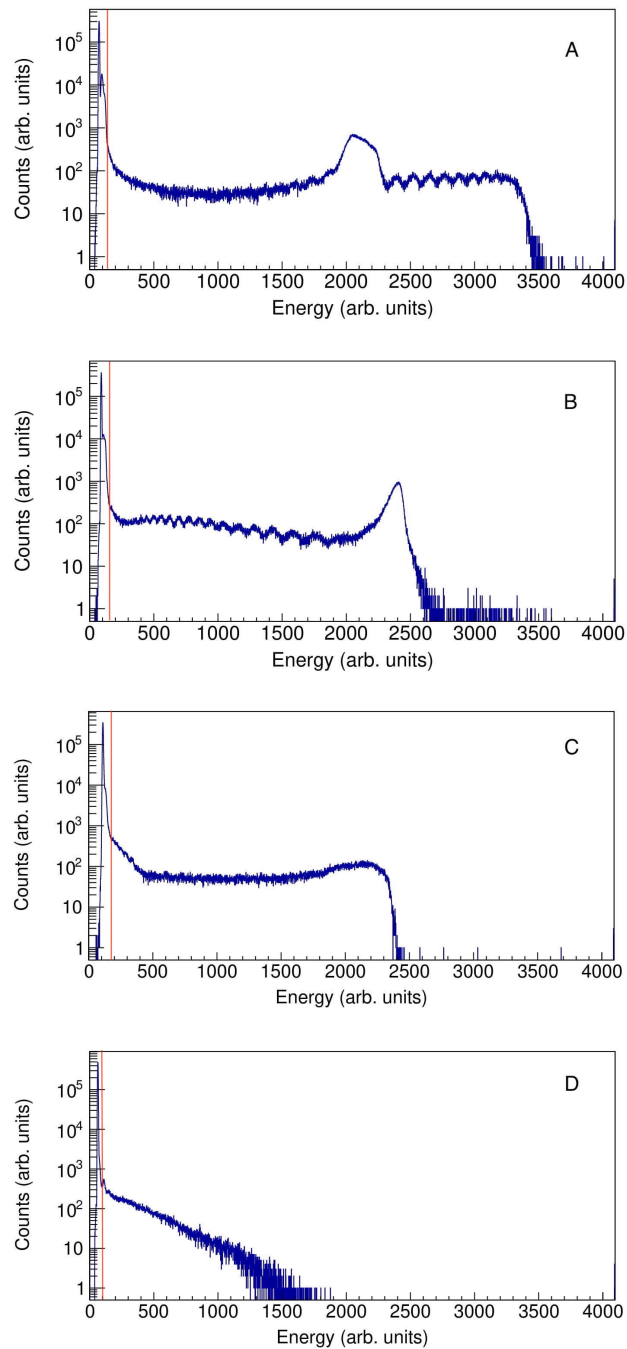
Figure 4.10: The raw spectra of the 4 sections composing one of the central rows of the IC. According to the Bethe formula, the Pb-like ions are stopped before Sn-like ions. The red line represents the threshold to eliminate the pedestal coming from the electronics.
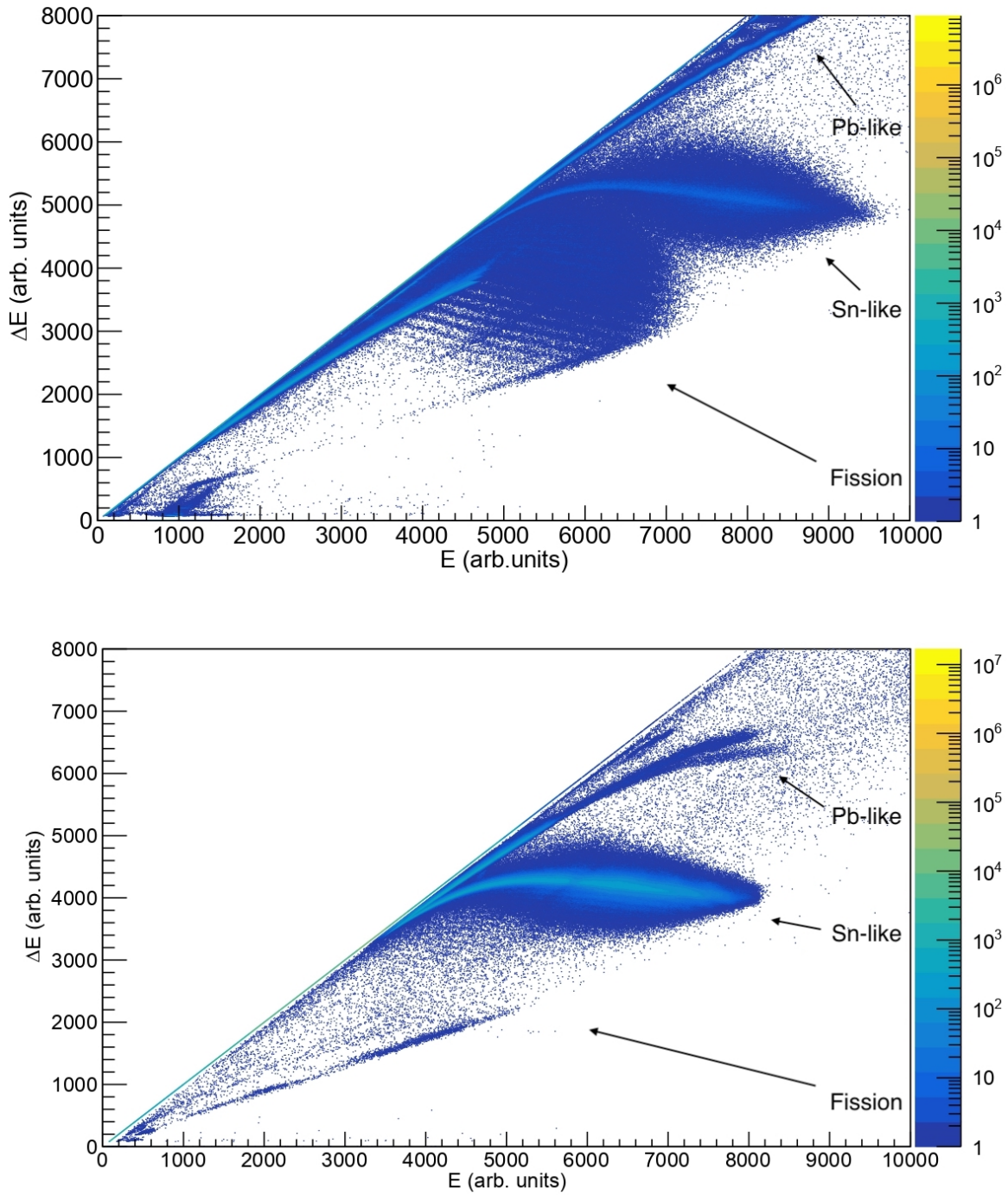
Figure 4.11: Energy loss in the first two IC layers ΔE_{AB} as a function of the total energy loss E_{IC} for the measurements at 25° (top) and 35° (bottom) degree of PRISMA. One can observe the yield of the Sn-like ions populated through the MNT reactions, Pb-like ions and fission fragments.

IC, are rejected (red). The ions fully stopped in the IC by means of the necessary gas pressure. This means the total energy of the recoil can be obtained by summing the energy of all sections. If the energy loss of the event is not consistent with the reconstructed trajectory, then they are rejected as well. The remaining events are considered valid for the analysis procedure (green).

The energy loss ΔE as a function of the total energy loss E for the measurements at both angles are shown in Figure 4.11. One can observe the most intense band corresponding to the yield of the Sn-like ions, the Pb-like ions close to the region where ΔE and E merge, and the fission fragments around Z $\sim$ 30-40.

The identification of the atomic numbers of the reaction products will be discussed in Section 4.3.

4.2.4   Trajectory reconstruction

The complete identification of the reaction fragments is based on the software reconstruction of the ion trajectories. The software, known as PRISMA manager routine, calculates the curvature radius ρ and the path length L of the ion trajectory which allow to derive the mass and the charge of the ions, see Section 4.2.2. In addition, this routine provides the range R and the total energy released E in the IC which can be used to identify the nuclear charge of the ions.

In order to reconstruct the trajectories the software uses the position, time and energy signals coming from the entrance detector and the focal plane detectors, and the equations of motion of a charged particle in the quadrupole and dipole magnetic fields. To calculate the trajectory in the analysis procedure of this experiment some approximations were necessary: the ions are emitted from the center of the target, the ion optical elements are considered to be ideal and the trajectories are planar in the xy plane of PRISMA frame of reference with a direction of incoming ions pointing towards x, see Figure 4.12.

A description of the equations of motion in the dipole and the quadrupole magnetic fields, and of the routine for the trajectory reconstruction will be given in the subsections below.

Quadrupole field

The entrance position of the ion in the quadrupole is defined by the coordinates returned from the MCP detector.
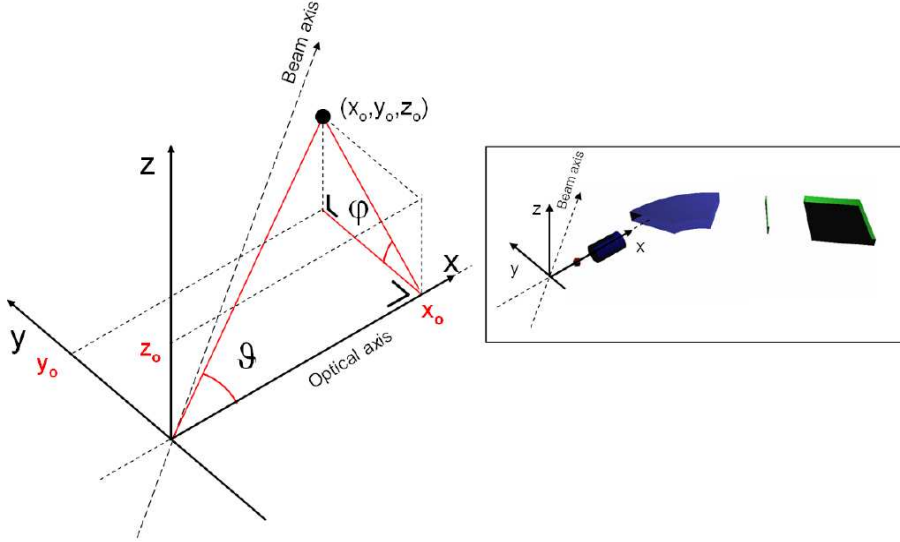
Figure 4.12: The reference frame of the PRISMA spectrometer [19].

In the ideal case, the quadrupole magnetic field is defined by the equation

$$\vec{B} = \vec{\nabla} U_m$$

where

$$U_m(y, z) = \frac{B_{max}}{\rho} yz$$

is the magnetic potential, and the force acting on a charged particle is derived from the Lorentz equation

$$\vec{F} = q\vec{v} \times \vec{B}$$

As a result, the magnetic force has two components:

$$F_y \simeq qv_x B_y(y, z)$$
$$F_z \simeq -qv_x z B_z(y, z)$$

In this way, the motion of the ion inside the quadrupole field is hyperbolic which focuses it in the vertical plane and defocuses in the horizontal plane. With known length of the quadrupole one can calculate the coordinates of the reaction fragments

leaving the quadrupole. The trajectories from the quadrupole to the dipole follow the straight line taking into account that the magnetic field is considered to be ideal.

Dipole field

The entrance coordinates of the ion in the dipole are determined by the previous equation of motion in the quadrupole field. Then the ion is deviated according to the Lorentz force within the dipole and it travels a circular motion with a radius ρ:

$$\rho = \frac{mv}{qB} \tag{4.4}$$

where m is the atomic mass, v is the tangential velocity of motion, q is the atomic charge and B is the magnetic field strength. Equation 4.4 governs the working principle of a spectrometer which deflects ions according to the their *magnetic rigidity*:

$$B\rho = \frac{mv}{q} = \frac{p}{q} \tag{4.5}$$

The trajectories of the ions exiting the dipole and going up to the MWPPAC are considered as straight lines since there is no magnetic force.

Reconstruction of the ion trajectories

Using the information provided by all the detectors and the equations of motion desctibed above one can reconstruct the total length L of the ion trajectory:

$$L = L_{MCP} + L_Q + L_{Q-D} + L_D + L_{MWPPAC}$$

where

- L_{MCP} is a straight line from the target to the entrance of quadrupole;

- L_Q is a hyperbolic path inside the quadrupole magnet;

- L_{Q-D} is a straight line from the exit of quadrupole to the entrance of dipole;

- L_D is a circular path in the horizontal disperson plane within the dipole magnet;

- L_{MWPPAC} is a straight line from the exit of dipole to the MWPPAC.

The total length L and the bending radius ρ of each particle are reconstructed iteratively using the ray-tracing algorithm of the PRISMA manager routine. The routine calculates the position on the focal plane taking into account the measured position on the MCP and a guess radius $\rho = 120$ cm corresponding to an ideal central trajectory. Then the calculated position is compared with measured one. The iterative procedure is continued until the calculated position matches the measured one with a difference of these two positions less than 1 mm by modifying the guess radius ρ towards the measured position.

After the trajectory reconstruction one can calculate the range R of the ion in the IC in the following way:

- all events with the path in the IC not consistent with the reconstructed trajectory are rejected;

- the total energy E of the ion is calculated by summing the measured energy losses ΔE_i in the different sections of the IC;

- a weighted distance L_w between the MWPPAC and each IC section is calculated by using ΔE_i as a weight;

- the range R is reconstructed by subtracting the MWPPAC-IC distance from the weighted distance L_w.

4.3 Identification of the Nuclear Charge

As it was mentioned before, the thesis is aimed at the nuclear charge Z identification of the target-like reaction products. This goal can be achieved by means of the IC measuring the energy loss and the total energy of the ions. The ions entering the IC deposit their kinetic energy by interactions with a gas filling the IC, see Section 3.3.4. The specific energy loss of an impinging particle in an absorber is governed by the Bethe–Bloch equation [40]:

$$ -\frac{dE}{dx} = \frac{4\pi e^4}{m_0} \frac{Z^2}{v^2} \; Nz \left[ln\left(\frac{2m_0 v^2}{W}\right) - ln\left(1 - \beta^2\right) - \beta^2 \right] \qquad (4.6) $$

where Z and v are the nuclear charge and the velocity of the incident particle, m_0 and e are rest mass and the charge of the electron respectively, N and z are the number density and the atomic number of the absorber atoms, W is an experimentally determined parameter which represents the average excitation and ionisation

potential of the absorber, β is the ratio between the velocity of the ion and the velocity of light. In the non-relativistic approximation Equation 4.6 becomes

$$-\frac{dE}{dx} \propto \frac{mZ^2}{E_{kin}} \, ln\left(\frac{E_{kin}}{m}\right) \tag{4.7}$$

where the term $E \times \frac{dE}{dx}$ weakly depends on the kinetic energy E_{kin} of the ion and can be used for the Z identification through the energy loss dE versus the total kinetic energy E_{kin} matrix. In addition, Z can be obtained with the total kinetic energy E_{kin} versus the range R matrix since the range R of the ion is defined as

$$R = \int_{E_{kin}}^{0} \left(-\frac{dE}{dx}\right)^{-1} \, dE. \tag{4.8}$$

In PRISMA manager routine ΔE and E correspond to dE and E_{kin} of the Bethe–Bloch equation, respectively.

Basing on the definition above the ΔE-E matrix will be constructed in order to identify the nuclear charge Z of the Sn-like transfer products of the ^{206}Pb+^{118}Sn reaction. Then Z distribution of these transfer products together with their absolute and relative intensities will be determined. A description of the performed procedure will be given in the subsections below.

Construction of Z spectra

Once the calibration procedure of the PRISMA detectors is performed one can plot the ΔE-E matrix using the valid events coming from the IC. Figure 4.13 (top and bottom) shows the energy loss in the first two rows of the IC against the full energy deposition in the IC of the transfer region measured with PRISMA placed at 25° and 35°, respectively. In both cases, it seems that the strong component of Sn ions (with elastic+inelastic transfer channels) overwhelm the various proton transfer channels making Z identification more difficult.

Figure 4.14 (left and right) shows the projection on the y axis of the transfer region of Sn-like ions rotated at a proper angle. One could naively assume that during the experiment the IC was not working properly since there is no peak relative to different nuclear charge. However, well-separated peaks of the fission products relative to different atomic charges in Figure 4.15 mean that there was no problem in the IC performance. Moreover, the experimental kinematics of the reaction is well matched with the calculated one reflecting that the Sn-like transfer products
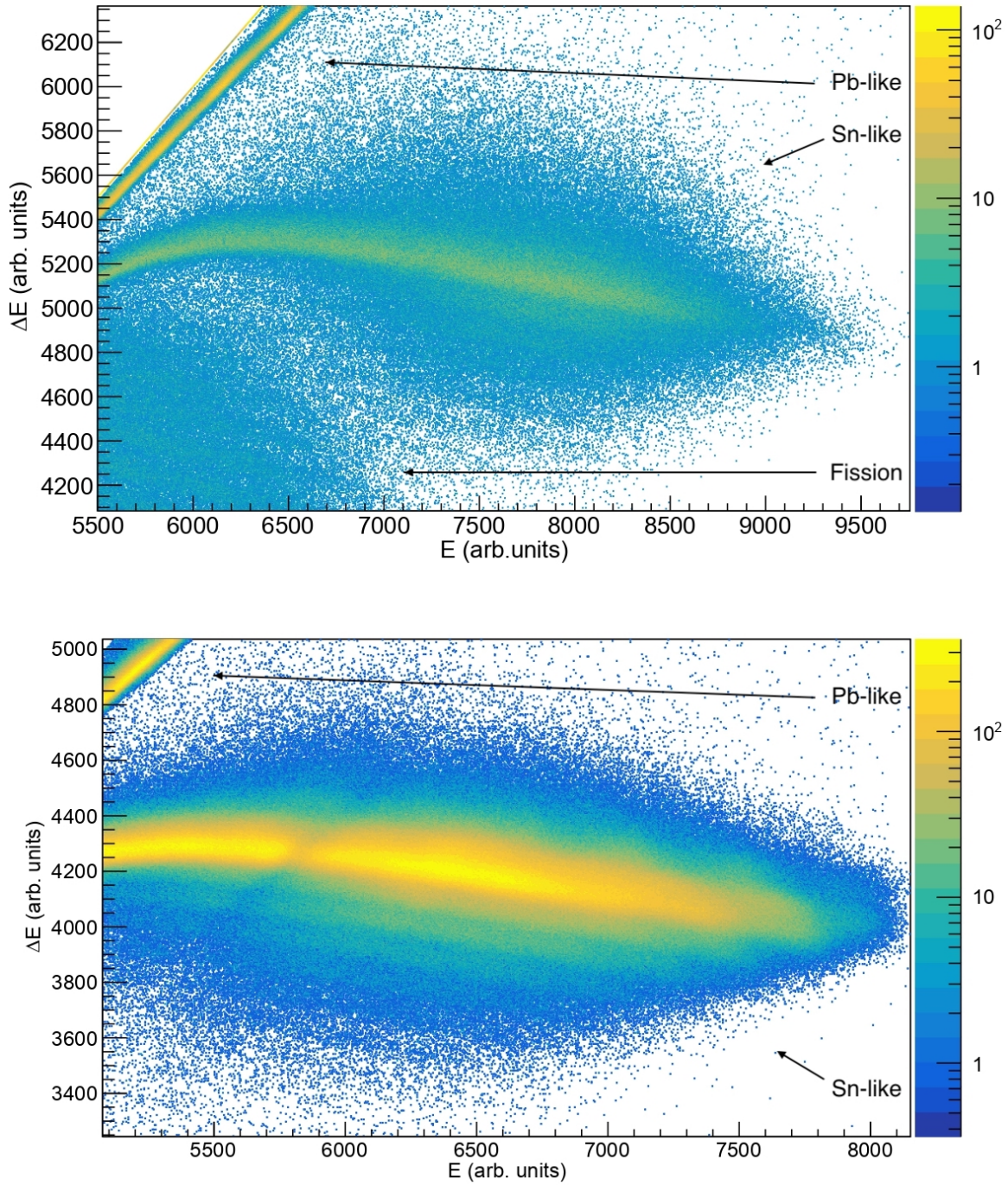
Figure 4.13: Energy loss in the first two IC layers (ΔE_{AB}) as a function of the total energy loss E_{IC} for the measurements of the transfer flux at 25° (top) and 35° (bottom) degree of PRISMA. One can note the the contribution of the strong component coming from the Pb-like ions.
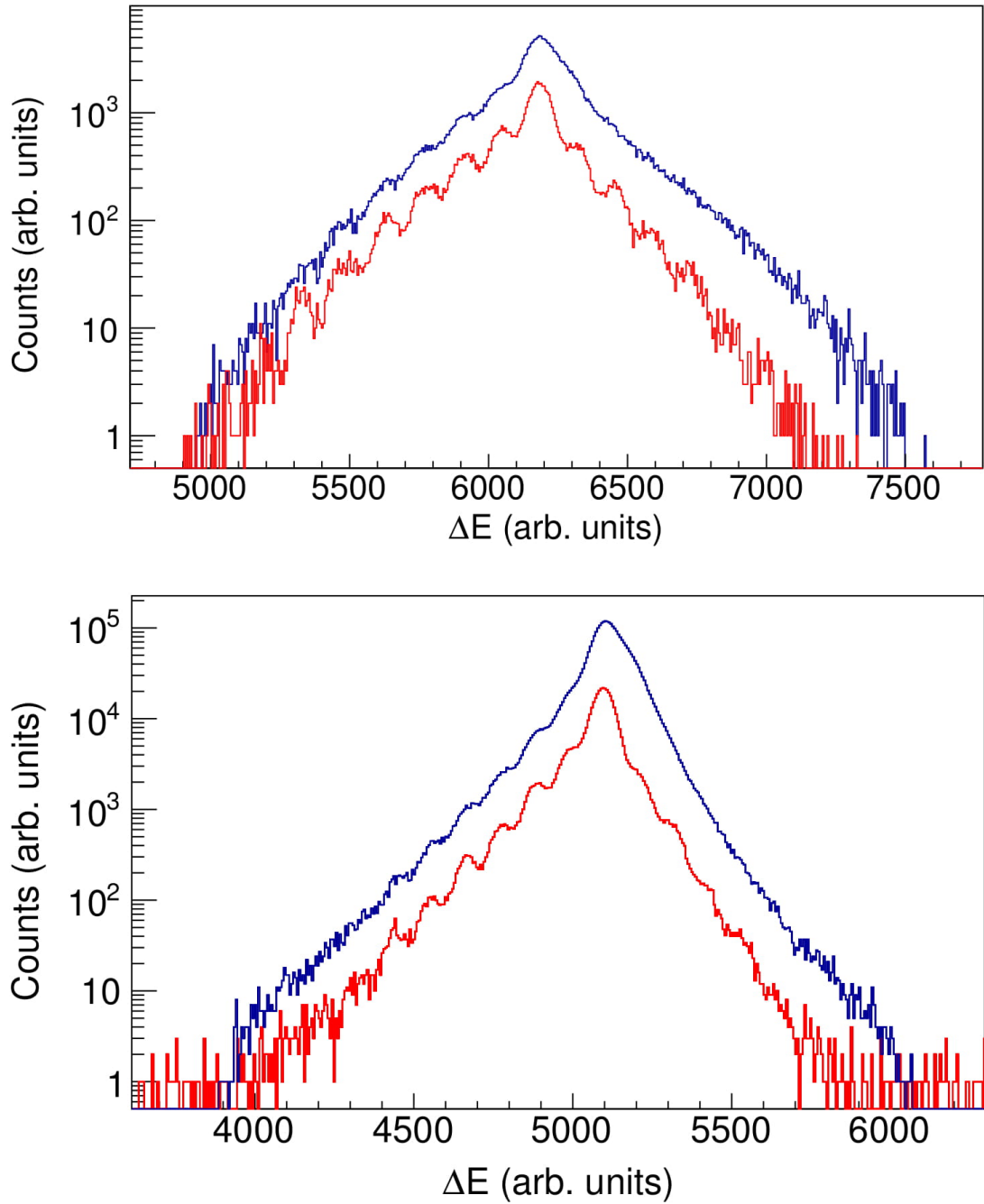
Figure 4.14: Projection on the y axis of the rotated ΔE-E matrix in the Sn-like transfer region for the measurements at 25° (top) 35° (bottom) of PRISMA. The original spectra are in blue. The final spectra are in red. See text for details.
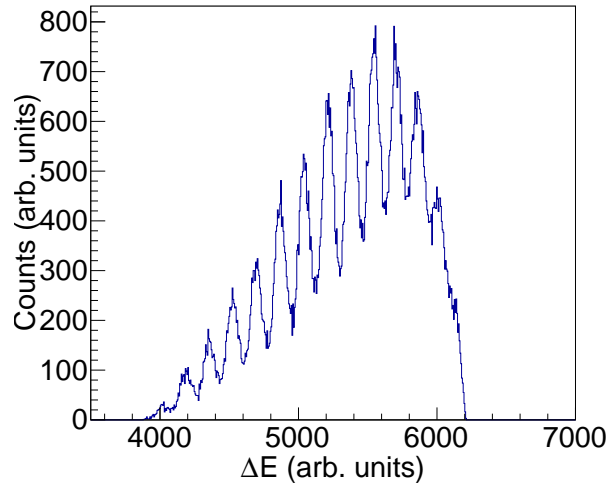
Figure 4.15: Projection on the y axis of the rotated ΔE-E matrix in the region of fission fragments (at 25 ° of PRISMA). This is a clear indication that that the resolution of the IC is good enough to distinguish various nuclear charges of fission fragments around Z = 30-40.

have high kinetic energies around 750 MeV to be detected with good enough Z resolution, see Figure 4.16. Summarizing the facts that there was no problem in the operation of the IC, the resolution of the IC is expected to be ΔZ/Z $\simeq$ 1/60 and the bombarding energy is well above the Coulomb barrier which increases the cross sections of proton transfer channels it is concluded that the partial determination of the different Z distributions should be possible. Therefore, one should check the calibration or gain matching between different sections of the IC which was carried out before the experiment, see Section 4.2.3. This is done through the following procedure:

- only the ions with straight trajectories in each of the 10 sections of the MWP-PAC and the IC (and without energy loss in the nearby sections) were selected;

- with the selected events ΔE-E matrix was plotted for each of these 10 sections;

- each ΔE-E matrix was rotated at a proper angle (the same for all ΔE-E matrices) and was projected on the y axis the transfer region of Sn-like ions

- the centroids of the projections were aligned with respect to each other introducing a small correction;

- all the corrected (and rotated) ΔE-E matrices with the selected events were summed to create a new ΔE-E matrix.
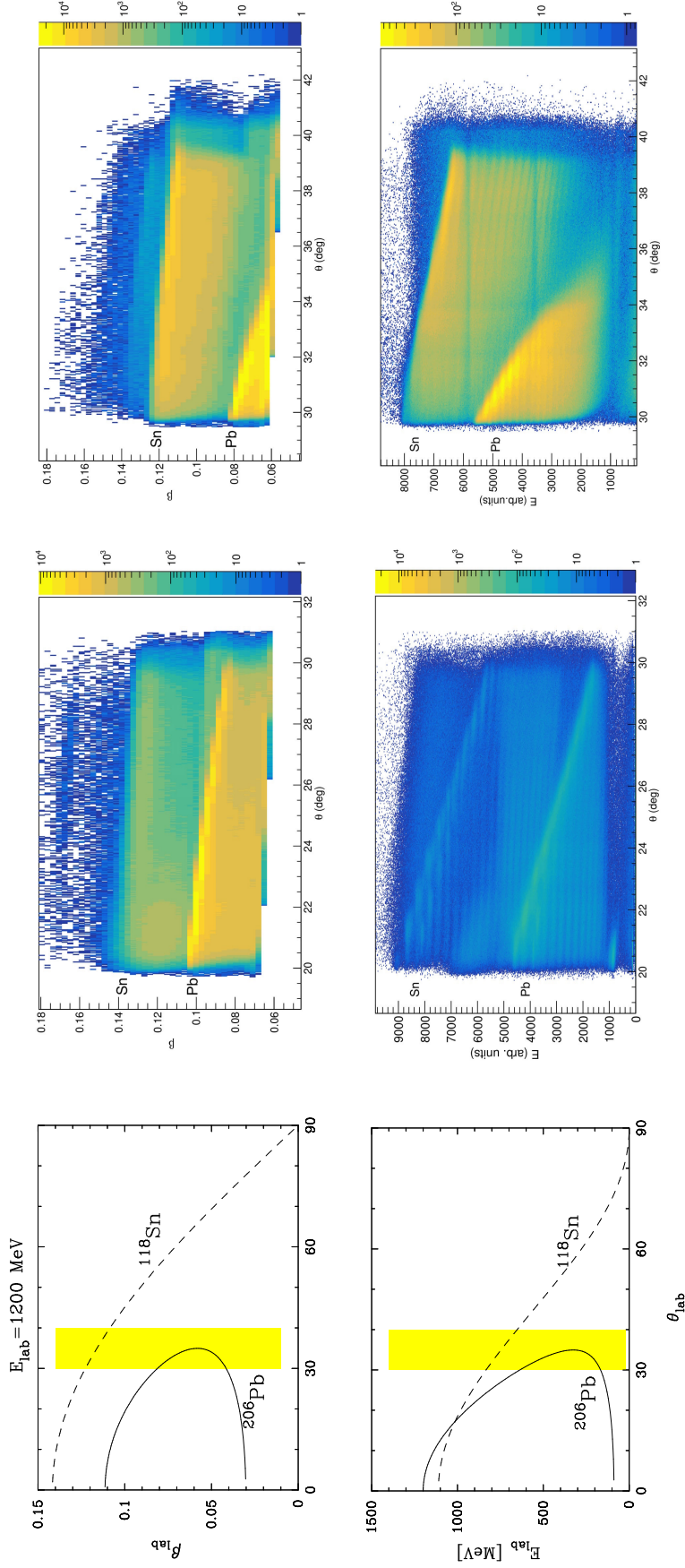
Figure 4.16: Calculated (left) and experimental kinematics of the ^{206}Pb+^{118}Sn reaction at E_{lab}=1200 MeV at 25° (middle) and 35° (right). The β=v/c (top) and the energy (bottom) of the indicated ions detected in PRISMA as a function of the scattering angle. All the trends are well matched. The shaded (yellow) region corresponds to the PRISMA acceptance at θ_{lab}=35° [9].

In addition to the procedure above, to reduce the contribution from Pb-like ions, the TOF gate for the Sn-like transfer region was applied to the both measurements at 25° and 35° of PRISMA. The final spectra of the ΔE-E matrix projected on the y axis are shown in Figure 4.14. One can see the clear improvement represented as the distinct peaks relative to different nuclear charges. By incorporating the ions with only straight trajectories the original spectra was reduced roughly by a factor 3 in both cases. A more detailed treatment of the nuclear charge Z selection process can be found in Ref. [18, 42].

Determination of Z distributions

The mass-integrated proton transfer channels are shown in Figure 4.17 ranging from (-7p) to (+6p) and from (-8p) to (+5p) for the measurements at 25° and 35° of PRISMA, respectively. In both cases, proton-stripping channels are populated more than the proton pick-up channels. The absolute yields of the these channels were extracted by means of the multigaussian fit. In this experiments, a Z resolution of about ΔZ/Z $\sim$ 1/68 was obtained.

The absolute and relative intensity distribution of the selected mass-integrated proton transfer channels is listed in Table 4.4. The most intense (0p) peak corresponds to the Sn-like ions. Taking it as a reference the other peaks were assigned to the corresponding nuclear charges [43].
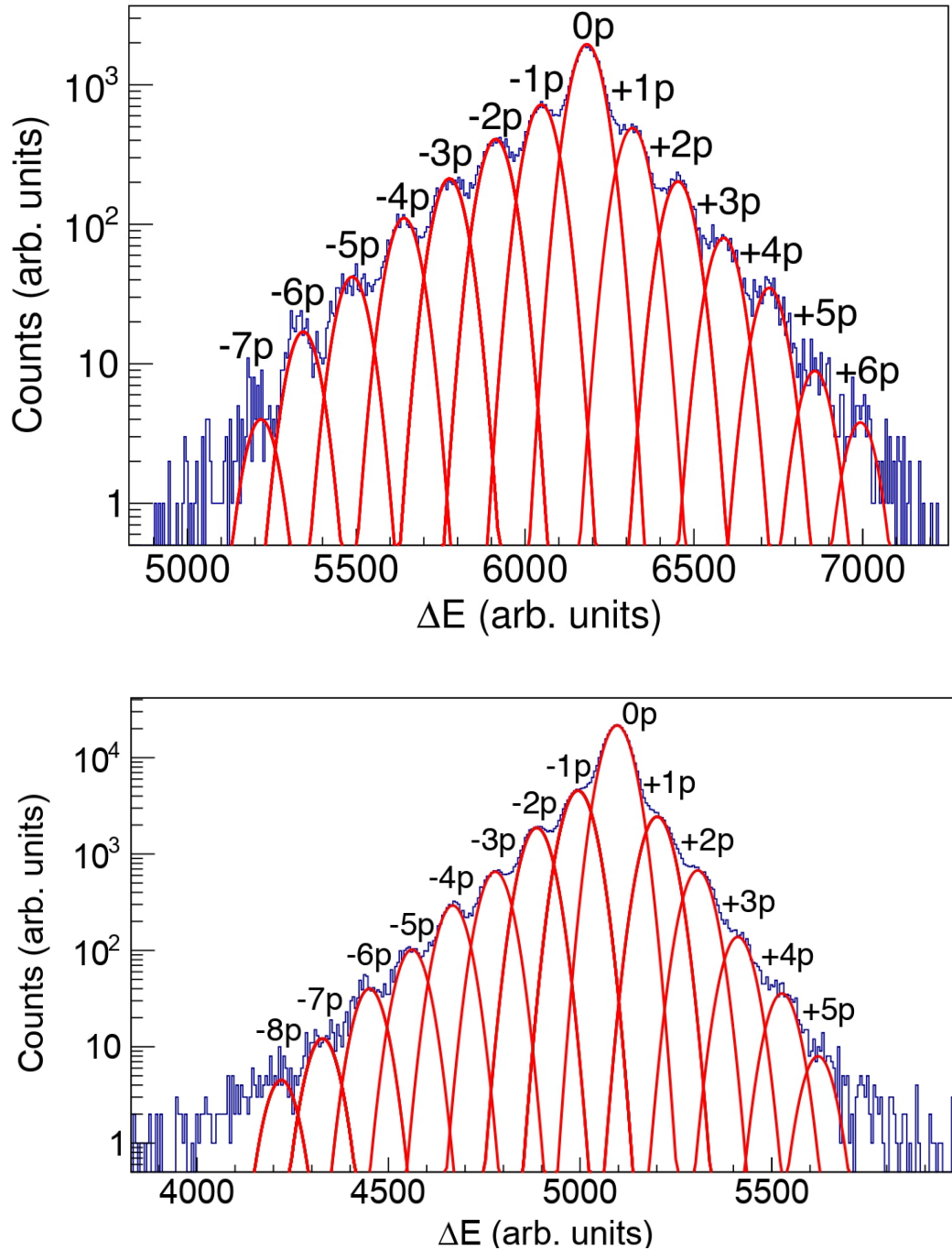
Figure 4.17: The final spectra showing the peaks corresponding to the mass-integrated proton channels for the measurements at 25° (top) and 35° (bottom) of PRISMA. The multigaussian fit used to extract the absolute yields for the indicated channels is represented by the red curves.

Table 4.4: Absolute (total amount of counts) and relative Z intensities of the Sn-like transfer products measured at 25° and 35° of PRISMA.

Z	Distribution	25°		35°	
42	Molybdenum (Mo)			0.35×10^3	0.02%
43	Technetium (Te)	0.42×10^3	0.20%	0.94×10^3	0.05%
44	Ruthenium (Ru)	1.79×10^3	0.87 %	3.37×10^3	0.18%
45	Rhodium (Rh)	4.41×10^3	2.14 %	8.57×10^3	0.47%
46	Palladium (Pd)	11.67×10^3	5.67 %	24.64×10^3	1.35%
47	Silver (Ag)	22.39×10^3	10.89 %	55.38×10^3	3.04%
48	Cadmium (Cd)	42.90×10^3	20.87 %	157.79×10^3	8.65%
49	Indium (In)	75.71×10^3	36.83 %	383.15×10^3	21.02%
50	Tin (Sn)	205.526×10^3	100 %	1822.76×10^3	100 %
51	Antimony (Sb)	51.52×10^3	25.06 %	205.84×10^3	11.29%
52	Tellurium (Te)	21.34×10^3	10.38 %	57.02×10^3	3.13%
53	Iodine (I)	8.41×10^3	4.09 %	11.64×10^3	0.64%
54	Xenon (Xe)	3.68×10^3	1.79 %	3.02×10^3	0.17%
55	Cesium (Cs)	0.93×10^3	0.45 %	0.67×10^3	0.04%
56	Barium (Ba)	0.39×10^3	0.19 %		

Chapter 5

Comparison of results with the Grazing code

As it was described in Section 2.2.3, the GRAZING code is based on the semi-classical model which treats the relative motion on a classical basis while inelastic excitations and transfers are treated in a microscopic way. The formalism lying behind the model can be found in Ref. [3, 44], while in this Section some of the approximations introduced in the description of the reaction will be outlined first. Then the interpretation of the nuclear charge distribution of the present system will be given by comparing with the theoretical model GRAZING and with other previously studied systems.

In the GRAZING model, a transition is characterized by several observables such as excitation energy E_i^*, number of neutrons N_i, number of protons Z_i and so on of the products. Then the model constructs the probability $P(E_a^*, E_A^*, N_a, Z_a, \cdots)$ of the given transition not by solving directly the semi-classical system of coupled equations 2.10 but by introducing a characteristic function:

$$P(E_a^*, \quad E_A^* \quad , N_a, Z_a, \cdots) = < \Psi(t)|\delta(\hat{H}_a - E_a^*) \cdots \delta(\hat{Z}_a - Z_a) \cdots |\Psi(t) > \quad (5.1)$$

where the Z function contains some parameters that have to be introduced if necessary. It is important to mention, without further discussion, that the transition probabilities are calculated following classical trajectories constructed in a self-consistent way so as to be compatible with the different quantities defining the final states [10].

In order to describe the relative motion and to calculate the inelastic form factors, GRAZING uses the following parametrization of the nuclear ion-ion potential [29]:

$$U_{aA}^N = -16\pi\gamma a\frac{R_a R_A}{R_a + R_A}\left[\frac{1}{1 + e^{(r-R_a-R_A)/a}}\right] \tag{5.2}$$

where $R_i = \left(1.20A_i^{1/3} - 0.09\right)$ fm are the nuclear radii of the two nuclei, the diffusion parameter a expressed as

$$\frac{1}{a} = 1.17\left(1 + 0.53(A_a^{-1/3} + A_A^{-1/3})\right) \quad \text{fm}^{-1} \tag{5.3}$$

and the surface tension γ is given by

$$\gamma = -0.95\left[1 - 1.8\frac{(N_a - Z_a)(N_A - Z_A)}{A_a A_A}\right] \quad \text{MeVfm}^{-2} \tag{5.4}$$

where A_i is the mass number and Z_i, N_i stands for the charge and neutron number respectively. For the Coulomb interaction the model uses the expression of two points charges.

In order to compare the experimental data with the calculations, it is necessary to extract the yields. By means of the multigaussian fit, as it is shown in Figure 4.17, the yield of each nuclear charge were obtained for the measurements at 25° and 35° of PRISMA. The experimental absolute cross sections were not measured with sufficient precision due to the lack of the information on the transmission of the spectrometer for the present experiment. Therefore, the calculations were used for the normalization of the experimental yield. The GRAZING model has been successfully reproducing a variety of experimental results with heavy ions. In particular, it describes well one-neutron and one-proton transfer channels (see Section 2.2.3). In our case, the (-1p) channel was chosen for the normalization due to the fact that the proton stripping path in the present experiment is better separated allowing to determine the yield with better precision. Finally, one obtains Figure 5.1 which shows the comparison of the experimental total cross sections for each mass-integrated proton transfer channel with the ones calculated by GRAZING.

Comparing the experimental data with the theory a list of observations are obtained:

- Theory well reproduces the (+1p) channel but there is a clear underestimation starting from the (-2p) and (+2p) channels in both pick-up and stripping paths. As it was mentioned in Section 2.2.3, the GRAZING calculations do not fully take into account the influence of the deep-inelastic components to
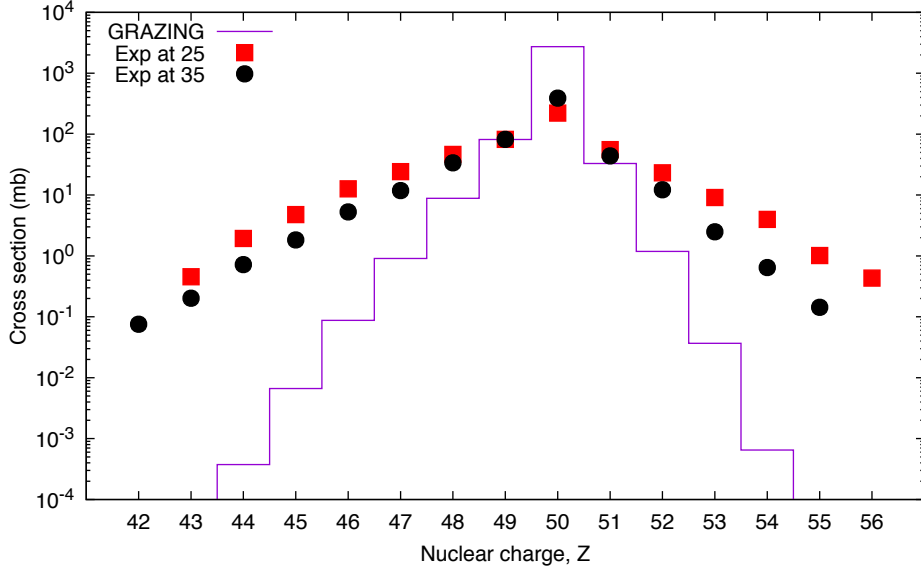
Figure 5.1: Comparison between experimental data measured at 25° (red square)
and 35° (black circle) of PRISMA and the GRAZING calculations for
mass-integrated proton transfer channels of the present experiment.

the reaction. The deviation from the calculation indicates that the fragment
isotopic distributions have large contributions associated with strong energy
damping in the deep-inelastic regime at this energy above the Coulomb barrier
(see Section 2.1.1). Similar underestimations of the GRAZING were observed
in the previously studied ^{40}Ar+^{208}Pb [19] and ^{197}Au+^{130}Te [18] reactions (see
Figure 5.2).

- One can note that in the measurement at 25° the deviation is more pronounced.
  This is a clear indication of the deep-inelastic components in the reaction
  dominating over the quasi-elastic one when moving from more backward to
  more forward angles.

- The behaviour of the distribution moving from 35° to 25° becomes more sym-
  metric. This can be considered as a n additional signature of the evolution of
  reaction from quasi-elastic to the more complex deep-inelastic regime.

- According to the GRAZING the proton stripping path is more favoured than
  the pick-up one. This behaviour is confirmed by the measurements at both
  angles.

- The GRAZING did not reproduce the (-7p), (-8p), (+5p) and (+6p) channels
  which were identified experimentally with quite small cross sections.

It is very suitable to make comparison between our ^{208}Pb+^{118}Sn reaction and the previously studied ^{197}Au+^{130}Te [18] reaction since the projectile-target combinations in these reactions have a similar mass asymmetry conditions. Therefore, the main parameter that defines the reaction is the bombarding energy. One can note that in our case the data are much more underpredicted by theory than the case of ^{197}Au+^{130}Te. This is most likely due to the fact that in case of the ^{197}Au+^{130}Te one used lower bombarding energy (close to the barrier) than in our case (above the barrier) so there are less deep-inelastic components contributing to the reaction. Referring to Figure 4.1, one can then expect that at even lower bombarding energies in our reaction, which correspond to larger distances of closest approach, one could have much less deep-inelastic components (and much more dominant quasi-elastic components) which would provide the best condition to study the nucleon-nucleon correlations.
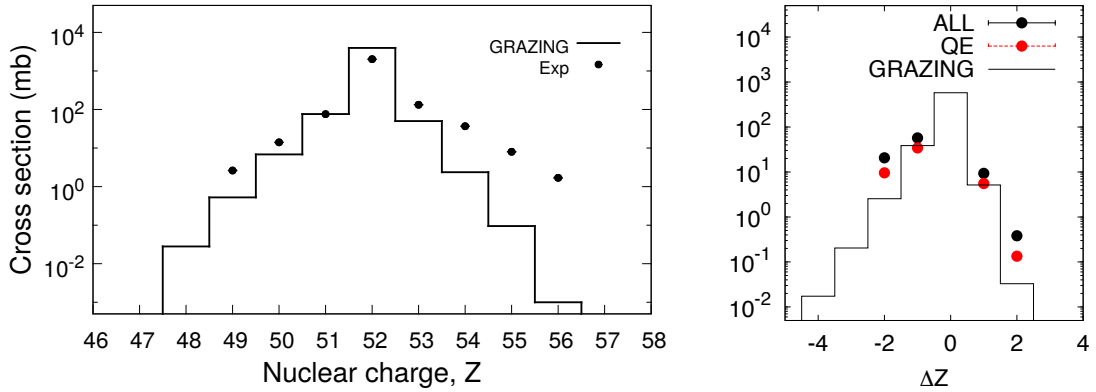
Figure 5.2: Right: The experimental (points) and the GRAZING (histogram) cross sections for mass integrated proton transfer channels of the reaction ^{197}Au+^{130}Te at E$_{lab}$ = 1.07 GeV [18].

Left: The total experimental cross sections (black points) and cross section of the quasi-elastic component (red points) for the pure proton transfer channels compared with the GRAZING calculations for the reaction ^{40}Ar+^{208}Pb at E$_{lab}$ = 260 MeV [19].

Thus, it would be very interesting and challenging to perform a future complete analysis of the reaction, in terms of both nuclear charge and mass distributions at all measured energies and in particular at the lowest ones where important information on nucleon-nucleon correlations could be extracted.

Chapter 6

Summary and outlook

In this thesis multinucleon transfer reactions were studied in the ^{206}Pb+^{118}Sn system in inverse kinematics, with the aim to the investigate the nucleon-nucleon correlations in the nuclear medium. The measurement of the transfer products was performed using the full performance of large acceptance PRISMA spectrometer which provides high resolution and efficiency allowing to extract the total cross sections of the various reaction channels.

The full analysis of this experiment would allow to study the evolution of the transfer probability as a function of the distance of closest approach for one and two neutron transfers, which was measured by varying the beam energy from above to well below the Coulomb barrier (E_{lab}=1200, 1090 and 1035 MeV) and the detection angle of the Sn-like transfer products (θ_{lab}=25° and 35°). The behavior of the transfer probabilities could provide information on the effect of the nucleon-nucleon correlations in the evolution of the reaction in the presence of high Coulomb field. For a proper comparison with already studied systems, the present system fulfills the requirements to be well Q-value matched for neutron transfer channels and to be detected with sufficient precision in A, Z and Q-value.

Among the used three bombarding energies the highest one corresponds to the highest kinetic energies of the reaction fragments and highest cross section of the transfer products, in particular for the proton transfer channels, with the best Z resolution in the IC. Therefore, this thesis was devoted to the identification of the nuclear charges of the Sn-like transfer products measured at the highest bombarding energy at both angles.

By means of a calibration procedure of all the detectors and the software tools used for the analysis of PRISMA data it was possible to extract the events related to the nuclear charges of the Sn-like fragments. Although the region of interest was

overwhelmed by the strong component coming from the elastically scattered Sn ions and was affected by the presence of the Pb-like ions which made the Z identification more difficult, after a sophisticated analysis procedure a Z resolution of about Δ Z/Z $\sim$ 1/68 was achieved. This allowed to extract the absolute yields of the mass-integrated proton transfer channels from (-7p) to (+6p) and from (-8p) to (+5p) for the measurements at 25° and 35°, respectively.

The extracted experimental yields were compared with the GRAZING model which has been successful in describing transfer reactions with lighter systems. The model well reproduces the (+1p) mass-integrated proton transfer channel. Moreover, the prediction that the proton stripping path is more favoured than the pick-up one was confirmed by the measurements at both angles. It was observed that our data are much more underestimated by the model than in the case of the previously studied ^{197}Au+^{130}Te [18] heavy system, having similar mass asymmetry conditions. The most likely explanation of this behavior is the use of higher bombarding energy in our case generating a much stronger contribution of the deep-inelastic components. In this way, it is expected that at lower bombarding energies, corresponding to larger distances of closest approach, the deep-inelastic components will be strongly reduced with a growth of the quasi-elastic ones providing the best condition for the nucleon-nucleon correlation studies.

To extract information on these nucleon-nucleon correlations one needs to distinguish pure proton and pure neutron transfer channels. Therefore, a complete identification of the transfer reaction products at all measured energies, and in particular at the lowest ones, becomes mandatory. In this context, the analysis procedure carried out in this thesis serves as a solid basis for future work.

Bibliography

[1] F. Galtarossa, L. Corradi, S. Szilner, E. Fioretto, G. Pollarolo, T. Mijatović, D. Montanari, D. Ackermann, D. Bourgin, S. Courtin, G. Fruet, A. Goasduff, J. Grebosz, F. Haas, D. Jelavi ć Malenica, S. C. Jeong, H. M. Jia, P. R. John, D. Mengoni, M. Milin, G. Montagnoli, F. Scarlassara, N. Skukan, N. Soić, A. M. Stefanini, E. Strano, V. Tokić, C. A. Ur, J. J. Valiente-Dobón, and Y. X. Watanabe. Mass correlation between light and heavy reaction products in multinucleon transfer ^{197}Au$+^{130}$Te collisions. *Physical Review C*, 97(7):054606, 2018.

[2] W. Królas. *Heavy-ion deep-inelastic collisions studied by discrete gamma-ray spectroscopy*. PhD thesis, University of Kraków, 1996.

[3] A. Winther. Dissipation, polarization and fluctuation in grazing heavy-ion collisions and the boundary to the chaotic regime. *Nuclear Physics A*, 594(2):203–245, 1995.

[4] S. Szilner, L. Corradi, G. Pollarolo, S. Beghini, B. R. Behera, E. Fioretto, A. Gadea, F. Haas, A. Latina, G. Montagnoli, F. Scarlassara, A. M. Stefanini, M. Trotta, A. M. Vinodkumar, and Y. Wu. Multinucleon transfer processes in ^{40}Ca+^{208}Pb. *Physical Review C*, 71(4):044610, 2005.

[5] T. Mijatović, S. Szilner, L. Corradi, D. Montanari, G. Pollarolo, E. Fioretto, A. Gadea, A. Goasduff, D. Jelavić Malenica, N. Mărginean, M. Milin, G. Montagnoli, F. Scarlassara, N. Soić, A. M. Stefanini, C. A. Ur, and J. J. Valiente-Dobón. Multinucleon transfer reactions in the ^{40}Ar+^{208}Pb system. *Physical Review C*, 94(6):064616, 2016.

[6] L. Corradi, S. Szilner, G. Pollarolo, G. Colo, P. Mason, E. Farnea, E. Fioretto, A. Gadea, F. Haas, D. Jelavić-Malenica, N. Mărginean, C. Michelagnoli, G. Montagnoli, D. Montanari, F. Scarlassar, N Soić, A. M. Stefanini, C. A.

Ur, and J. J. Valiente-Dobón. Single and pair neutron transfers at sub-barrier energies. *Physical Review C*, 84(3):034603, 2011.

[7] D. Montanari, L. Corradi, S. Szilner, G. Pollarolo, E. Fioretto, G. Montagnoli, F. Scarlassara, A. M. Stefanini, S. Courtin, A. Goasduff, F. Haas, D. Jelavić Malenica, C. Michelagnoli, T. Mijatović, N Soić, C. A. Ur, and M. Varga Pajtler. Neutron Pair Transfer in ^{60}Ni+^{116}Sn Far below the Coulomb Barrier. *Physical review letters*, 113(5):052501, 2014.

[8] A. Winther. Winther A program GRAZING. http://personalpages.to.infn.it/~nanni/grazing/.

[9] L. Corradi, S. Szilner, et al. Nucleon-nucleon pairing correlations probed in the ^{206}Pb(^{118}Sn,$^{118+X}$Sn)$^{206-X}$Pb transfer reaction at far sub-barrier energies PRISMA. Proposal of the experiment, 2015.

[10] L. Corradi, G. Pollarolo, and S. Szilner. Multinucleon transfer processes in heavy-ion reactions. *Journal of Physics G: Nuclear and Particle Physics*, 36:113101–113143, 2009.

[11] A. Lombardi, G. Bassato, A. Battistella, M. Bellato, G. Bezzon, L. Bertazzo, C. Bisoffi, E. Bissiato, S. Canella, M. Cavenago, F. Cervellera, A. Chiurlotto, M. Comunian, A. Facco, P. Favaron, G. Fortuna, S. Gambalonga, M. Lollo, M. S. Moisio, V. Palmieri, R. Pengo, A. Pisent, M. Poggi, A. M. Porcellato, F. Scarpa, and L. Ziomi. The new positive ion injector PIAVE at LNL. In *Particle Accelerator Conference, 1997. Proceedings of the 1997*, volume 1, pages 1129–1131. IEEE, 1997.

[12] G. Fortuna, A.M. Porcellato, G. Bassato, A. Battistella, M. Bellato, L. Bertazzo, G. Bezzon, G. Bisoffi, G. Buso, S. Canella, M. Cavenago, F. Cervellera, A. Chiurlotto, A. Dainelli, N. Dainese, M. De Lazzari, A. Facco, P. Favaron, M. Lollo, A. Lombardi, S. Marigo, M. S. Moisio, V. Palmieri, R. Pengo, M. Poggi, J. S. Sokolowski, L. Badan, M. Barbadillo, R. Pegoraro, R. Preciso, and F. Scarpa. Completion of the medium-β section of the ALPI SC-booster at LNL. *Nuclear Instruments and Methods in Physics Research Section A: Accelerators, Spectrometers, Detectors and Associated Equipment*, 328(1):236–241, 1993.

[13] A. Latina. *Study of Heavy-Ion Reactions with the Magnetic Spectrometer PRISMA: On-line and Off-line Data Analysis.* PhD thesis, Università degli Studi di Torino, 2005.

[14] Philipp Rudolf John. *Study of shape evolution in the neutron-rich osmium isotopes with the advanced gamma-tracking array AGATA.* PhD thesis, Università di Padova, 2015.

[15] G. Montagnoli, A. M. Stefanini, M. Trotta, S. Beghini, M. Bettini, F. Scarlassara, V. Schiavon, L. Corradi, B. R. Behera, E. Fioretto, A. Gadea, A. Latina, S. Szilner, L. Donà, M. Rigato, N. A. Kondratiev, A. Yu. Chizhov, G. Kniajeva, E. M. Kozulin, I. V. Pokrovskiy, V. M. Voskressensky, and D. Ackermann. The large-area micro-channel plate entrance detector of the heavy-ion magnetic spectrometer PRISMA. *Nuclear Instruments and Methods in Physics Research Section A: Accelerators, Spectrometers, Detectors and Associated Equipment*, 547(2):455–463, 2005.

[16] S. Beghini, L. Corradi, E. Fioretto, A. Gadea, A. Latina, G. Montagnoli, F. Scarlassara, A. M. Stefanini, S. Szilner, M. Trotta, and A. M. Vinodkumar. The focal plane detector of the magnetic spectrometer PRISMA. *Nuclear Instruments and Methods in Physics Research Section A: Accelerators, Spectrometers, Detectors and Associated Equipment*, 551(2):364–374, 2005.

[17] S. Szilner. Private Communication, 2019.

[18] F. Galtarossa. *Multinucleon transfer in the $^{197}Au+^{130}Te$ reaction studied with a high-resolution kinematic coincidence.* PhD thesis, Università degli Studi di Ferrara, 2016.

[19] T. Mijatović. *Study of heavy-ion reactions with large solid angle magnetic spectrometers.* PhD thesis, Ruđer Bošković Institute, 2015.

[20] W. Von Oertzen, H. G. Bohlen, B. Gebauer, R. Künkel, F. Pühlhofer, and D. Scühll. Quasi-elastic neutron transfer and pairing effects in the interaction of heavy nuclei. *Zeitschrift für Physik A Atomic Nuclei*, 326(4):463–481, 1987.

[21] W. Von Oertzen and A. Vitturi. Pairing correlations of nucleons and multinucleon transfer between heavy nuclei. *Reports on Progress in Physics*, 64(10):1247, 2001.

[22] G. Pollarolo. Role of transfer reactions in heavy-ion collisions at the Coulomb barrier. *EPJ Web of Conferences*, 17(17):08002, 2011.

[23] R. Bass. Nuclear reactions with heavy ions. 1980.

[24] C. H. Dasso, G. Pollarolo, and A. Winther. Systematics of isotope production with radioactive beams. *Physical review letters*, 73(14):1907, 1994.

[25] R. Broda. Spectroscopic studies with the use of deep-inelastic heavy-ion reactions. *Journal of Physics G: Nuclear and Particle Physics*, 32(6):R151, 2006.

[26] J. M. Quesada, G. Pollarolo, R. A. Broglia, and A. Winther. A simple parametrization of one-particle transfer form factors for heavy-ion reactions. *Nuclear Physics A*, 442(2):381–396, 1985.

[27] A. B. Brown, C. W. Snyder, W. A. Fowler, and C. C. Lauritsen. Excited States of the Mirror Nuclei, ^{7}Li and^{7}Be. *Physical Review*, 82(2):159, 1951.

[28] L. Corradi, A. M. Vinodkumar, A. M. Stefanini, E. Fioretto, G. Prete, S. Beghini, G. Montagnoli, F. Scarlassara, G. Pollarolo, F. Cerutti, and A. Winther. Light and heavy transfer products in ^{58}Ni+^{208}Pb at the Coulomb barrier. *Physical Review C*, 66(2):024606, 2002.

[29] Ricardo A. Broglia and Aage Winther. Heavy ion reactions. 1991.

[30] Legnaro National Laboratories webpage. https://www.lnl.infn.it/index.php/en/.

[31] A. Pisent and M. Comunian. Complete simulation of the heavy ion Linac PIAVE. In *Particle Accelerator Conference, 1997. Proceedings of the 1997*, volume 1, pages 1132–1134. IEEE, 1997.

[32] A. Lombardi. The Superconducting Radio Frequency Quadrupole Structures Review. *Part. Accel.*, 62:91–102, 1998.

[33] G. Bassato, G. P. Buso, F. Cervellera, A. Dainelli, A. Facco, P. Favaron, G. Fortuna, J. D. Larson, V. Palmieri, R. Pengo, A. M. Porcellato, K. Rudolph, B. Tiveron, I. Ben-Zvi, and J. S. Sikolowski. The Alpi project at the Laboratori Nazionali di Legnaro. In *European particle accelerator conference*, 1988.

[34] G. Fortuna, R. Pengo, G. Bassato, I. Ben-Zvi, J. D. Larson, J. S. Sokolowski, L. Badan, A. Battistella, G. Bisoffi, G. Buso, M. Cavenago, F. Cervellera, A. Dainelli, A. Facco, P. Favaron, A. Lombardi, S. Marigo, M. S. Moisio, V. Palmieri, A. M. Porcellato, K. Rudolph, R. Preciso, and B. Tiveron. The ALPI project at the Laboratori Nazionali di Legnaro. *Nuclear Instruments and Methods in Physics Research Section A: Accelerators, Spectrometers, Detectors and Associated Equipment*, 287(1):253–256, 1990.

[35] A. Dainelli, G. Bassato, A. Battistella, M. Bellato, A. Beltramin, L. Bertazzo, G. Bezzon, G. Bisoffi, L. Boscagli, S. Canella, D. Carlucci, F. Cervellera, A. Chiurlotto, T. Contran, M. De Lazzari, A. Facco, P. Favaron, G. Fortuna, S. Gustafsson, M. Lollo, A. Lombardi, S. Marigo, M. S. Moisio, V. Palmieri, R. Pengo, A. Pisent, M. Poggi, F. Poletto, A. M. Porcellato, and L. Ziomi. Commissioning of the ALPI post-accelerator. *Nuclear Instruments and Methods in Physics Research Section A: Accelerators, Spectrometers, Detectors and Associated Equipment*, 382(1):100–106, 1996.

[36] A. M. Stefanini, L. Corradi, G. Maron, A. Pisent, M. Trotta, A. M. Vinodkumar, S. Beghini, G. Montagnoli, F. Scarlassara, G. F. Segato, A. De Rosa, G. Inglima, D. Pierroutsakou, M. Romoli, M. Sandoli, G. Pollarolo, and A. Latina. The heavy-ion magnetic spectrometer PRISMA. *Nuclear Physics A*, 701(1):217–221, 2002.

[37] H. Savajols. VAMOS: A variable mode high acceptance spectrometer for identifying reaction products induced by SPIRAL beams. *Nuclear Instruments and Methods in Physics Research Section B: Beam Interactions with Materials and Atoms*, 204:146–153, 2003.

[38] M. Rejmund, B. Lecornu, A. Navin, C. Schmitt, S. Damoy, O. Delaune, J.M. Enguerrand, G. Fremont, P. Gangnant, L. Gaudefroy, et al. Performance of the improved larger acceptance spectrometer: VAMOS++. *Nuclear Instruments and Methods in Physics Research Section A: Accelerators, Spectrometers, Detectors and Associated Equipment*, 646(1):184–191, 2011.

[39] A. Cunsolo, F. Cappuzzello, A. Foti, A. Lazzaro, A. L. Melita, C. Nociforo, V. Shchepunov, and J. S. Winfield. Technique for 1st order design of a large-acceptance magnetic spectrometer. *Nuclear Instruments and Methods in Physics Research Section A: Accelerators, Spectrometers, Detectors and Associated Equipment*, 481(1):48–56, 2002.

[40] G. F. Knoll. Radiation detection and measurement. *New York, John Wiley and Sons, Inc.*, 1, 1979.

[41] D. Montanari. *Reaction dynamics of neutron rich nuclei in Ca isotopes with heavy ions and gamma spectroscopy.* PhD thesis, Università degli Studi di Milano, 2009.

[42] B. Birkenbach. *Gamma ray tracking with the AGATA demonstrator - A novel approach for in-beam spectroscopy.* PhD thesis, Universiät zu Köln, 04 2014.

[43] Nuclear Data Center. https://www.nndc.bnl.gov/nudat2//.

[44] A. Winther. Grazing reactions in collisions between heavy nuclei. *Nuclear Physics A*, 572(1):191–235, 1994.